Third Worldwide Occurrence of Juangodoyite, Na₂Cu(CO₃)₂, and Other Secondary Na, Cu, Mg, and Ca Minerals in the Fore-Sudetic Monocline (Lower Silesia, SW Poland)

Łukasz Kruszewski [1],*, Mateusz Świerk [2], Rafał Siuda [3], Eligiusz Szełęg [4] and Beata Marciniak-Maliszewska [3]

[1] Institute of Geological Sciences, Polish Academy of Sciences, Twarda 51/55 Str., 00-818 Warszawa, Poland

[2] Faculty of Earth Sciences and Environmental Management, University of Wrocław, Plac Maksa Borna 9, 50-204 Wrocław, Poland; mateusz.swierk.1994@gmail.com

[3] Institute of Geochemistry, Mineralogy and Petrology, Faculty of Geology, University of Warsaw, Żwirki i Wigury 93 Str., 02-089 Warsaw, Poland; rsiuda@uw.edu.pl (R.S.); b.maliszewska@uw.edu.pl (B.M.-M.)

[4] Faculty of Natural Sciences, University of Silesia, Będzińska 60 Str., 41-205 Sosnowiec, Poland; eligiusz.szeleg@us.edu.pl

* Correspondence: lkruszewski@twarda.pan.pl

Abstract: Na-Cu carbonates are relatively rare secondary minerals in weathering zones of ore deposits. Hereby we describe mineral composition and crystal chemistry of the most important secondary (Na)Cu minerals and their Na- and Mg-bearing associates forming rich paragenesis in Rudna IX mine. A non-bulky Ca-rich dripstone-like paragenesis from Lubin Główny mine is also characterized, using Powder X-Ray Diffraction, Rietveld, and Electron Microprobe methods. Light blue juangodoyite (3rd occurrence worldwide) and darker chalconatronite are the most important members of the Rudna IX paragenesis, being associated with malachite, aragonite (intergrown with hydromagnesite and northupite), and probably cornwallite. Most of the minerals are chemically close to their ideal composition, with minor Mg substitution in malachite. Cu chlorides are mainly represented by clinoatacamite and probably herbertsmithite. Additional, minor phases include trace Cu minerals langite, wroewolfeite, and a lavendulan-group mineral, and monohydrocalcite. Separate halite-rich encrustations are shown to be filled with eriochalcite, ktenasite, and kröhnkite. The most likely to be confirmed coexisting species include paratacamite, wooldridgeite/nesquehonite, johillerite, melanothallite, and kipushite. The Lubin paragenesis mainly comprises aragonite, gypsum, rapidcreekite, and monohydrocalcite, with trace vaterite. Blue colouration is mainly provided by a yet unspecified Ni-, Co-, Mg-, and Mn-bearing Cu-Zn-Ca arsenate mineral close to parnauite.

Keywords: juangodoyite; chalconatronite; secondary Cu minerals; rapidcreekite; Fore-Sudetic monocline

1. Introduction

Juangodoyite, Na₂Cu(CO₃)₂ (monoclinic, *P*2₁/*a*), is an exceedingly rare mineral, known—prior to the current study—from a single locality in Chile: Santa Rosa mine, Iquique Province [1]. It is the natural equivalent of sodium di(carbonato)cuprate(II), named to honour Juan Godoy—the discoverer of the famous Chilean silver occurrence at Chañarcilllo. The synthetic equivalent of juangodoyite is obtained as small pinacoids, with dimensions ~0.1 mm, slightly elongated along the *c* axis, and somewhat irregular [2]. The hydrated, or trihydrate, counterpart of juangodoyite—chalconatronite (monoclinic, *P*2₁/*n*)—is more common, with about 20 localities worldwide. Its structure was analyzed

by Mosset et al. [3]. A second occurrence of juangodoyite, within drainage-related mine speleothems (minothems) of the Libiola Mine, Italy, was reported in Reference [4].

Chalconatronite occurrences are restricted to specific geochemical conditions. Its type locality is in Egypt, with genesis partially being related to saline groundwaters [5]. Further occurrences include the listed Chilean one [6]; Carr Boyd mine, Western Australia [7]; Zunderwand, Erlacher Bock area, Carinthia, Austria [8]; Geister vein of the Rovnost mine in the famous Czech uranium deposit at Jáchymov [9]; and salt mine at Bex, Vaud, Switzerland [10]. Few German localities are also known: Richeldsdorf area, Hersfeld-Rotenburg, Hesse [11]; Ludwig-Rudolf mine in Braulage [11] and Glücksrad mine, Oberschulenberg, Clausthal-Zellerfeld [12] of Goslar area, Lower Saxony; Braubach (e.g., [13]) and Friedrichssegen mine in Frücht [14] of Bad Ems area, Rhineland-Palatinate; Ramsbeck area, Meschede, Hochsauerlandkreis, Arnsberg, Nordrhine-Palatinate [11]; and in Saxony [15]. At least four USA sites are also known: Deremo mine, San Miguel County, Colorado [16]; Centennial mine, Centennial, Houghton Co. [17,18] and White Pine mine, Ontonagon County [19], Michigan; and Markey mine, San Juan County, Utah [20]. A recent Spanish discovery of chalconatronite at Eureka mine (Castell-estaó, La Vall Fosca, Lleida area, Catalonia) by Desor is also noteworthy [21]. Most of the above localities are polymetallic ore deposits or smelter slags related to them. Chalconatronite is, however, also known from alkaline magmatic rocks of the famous Mont Saint-Hilaire locality in Canada [22]. Interestingly, the holotype chalconatronite would not likely meet the current definition of a true mineral, as recommended by the International Mineralogical Association, as it was found as a patina on a bronze artifact, where it coexists with cuprite and atacamite [4].

Rapidcreekite is a mineral representing Cu-free, Ca-rich chemical system. With the $Ca_2(SO_4)(CO_3)\cdot4H_2O$ formula, this orthorhombic (*Pcnb*) is a mineral that may be treated as a chemical intermediate placed between aragonite and gypsum, though being more hydrated. Indeed, the Powder X-Ray Diffraction (PXRD) pattern of rapidcreekite is similar to that of gypsum and the twinning of the latter coupled with carbonate substitution gives a rapidcreekite motif [23]. With about 10 currently confirmed occurrences worldwide, rapidcreekite is more scarce than chalconatronite. The intermediate character of rapidcreekite in relation to $CaCO_3$ polymorphs and gypsum crystallization is discussed, e.g., by Bots [24]. At the type locality, Rapid Creek (hence the name), located within Dawson mining district, Yukon, Canada, rapidcreekite coexists with gypsum and aragonite, and results from supergene weathering [25]. The mineral is also known from the nearby Big Fish River site, well known for its well-crystallized, rare phosphate minerals, and another nearby site at Crosscut Creek in the Kulan Camp area [26]. Two occurrences are known from Germany: Johann mine in Burgfelsen, Wittichen/Schenkenzell area, Baden-Württemberg [27], where it coexists with very rare arsenate camgasite, $CaMg(AsO_4)(OH)\cdot5H_2O$, and also calcite, monohydrocalcite, gypsum, in the crust on a hydrothermally altered granite with Co and U mineralization; and Jeremias Glück mine in Garnsdorf, Saalfeld-Rudolstadt area, Thuringia [28]. At the latter site, Silurian alum shales were mined for the production of sulfuric acid and colored sulfate sinters were formed. Rapidcreekite is also known from other typical metal ore deposits, like that in the Esperanza mine, Lavrion area, Greece [29] and Mildigkeit mine of the Overberget Mining Field, Kongsberg, Buskerud, Norway [30]. At the latter site, it resides in calcite veins. It may also be a cave mineral, as is true for the hot spring-containing Diana Cave in Romania [31] where it forms in H_2S-rich environments in the course of H_2SO_4-driven weathering. Salama et al. report rapidcreekite, alongside gypsum, anhydrite, calcite, and nitratine ($NaNO_3$), in microbially mediated Egyptian ironstones [32]. The occurrence of rapidcreekite in the Lubin Główny mine is not unique for Poland. Warchulski et al. report its presence in pyrometallurgical slags of the Orzeł Biały smelting plant, Upper Silesia [33].

The primary mineralization of the Fore-Sudetic Monocline is related to the main four lithostratigraphic units: Weissliegend clastics, Boundary Dolomite, Kupferschiefer and Zechstein Limestone [34]. The sedimentary series is non-homogenous. The most common ore type is a disseminated one. Relatively common types also include veinlets, nests, lenses, and compact or laminated ones. The deposits are of a stratoidal type [35]. The crystallization of secondary minerals in

underground galleries of Cu mines of the Fore-Sudetic Monocline is connected with the oxidation of primary copper sulfides (mainly chalcopyrite, chalcocite and bornite). The released Cu^{2+} ions react with mine waters rich in chlorides and sulphates or with carbonates contained in ore bearing rocks. This process leads to formation of numerous interesting mineral species. In total, about 30 supergene minerals were described from these mines [36,37]. The most common are hydroxyhalides (e.g., botallackite, atacamite, clinoatacamite, paratacamite) and Cu sulfates (e.g., chalcanthite). Secondary arsenates (annabergite, erythrite, and possibly geminite) and carbonates (cerussite, malachite, azurite, and chalconatronite) are much less common [38].

This preliminary paper approximates mineralogical composition and mineral chemistry of Na-Cu carbonates and their major associates derived from the Rudna IX mine. Attention is also paid to Ca-rich paragenesis from the Lubin Główny mine. Selected results of related to the current study were shown in a conference [39]. Further studies including field, geochemical, and a more detailed crystallochemical research are planned.

2. Materials and Methods

The locations of the Rudna IX and Lubin Główny mines against the Fore-Sudetic Monocline and Poland are shown in Figure 1. The sampling points of the Lubin minerals under scope are shown in Figure 2.

Samples of the Rudna IX mine come from mine field No. 23 at a site located at the depth of ca. 1100 m below ground level. Here, the chalcocite-rich mineralization under scope occurs at a point of contact between sandstones and Cu-bearing shale. In the Lubin Główny mine, mineral samples were collected from mining excavations located in a vicinity of Chamber C1B. Here, flowstones are developed in places where groundwaters outflow from laminated dolostone contacting with sandstone layers. The samples include thin blue encrustations (up to several centimeters in diameter) on sandstones and dolostones covered by gray (locally white) protrusions. The protrusions may reach ~3.8 mm in height and comprise intergrown, gray crystals. Single, colorless, clearly monoclinic crystals are also found disseminated within the blue portions.
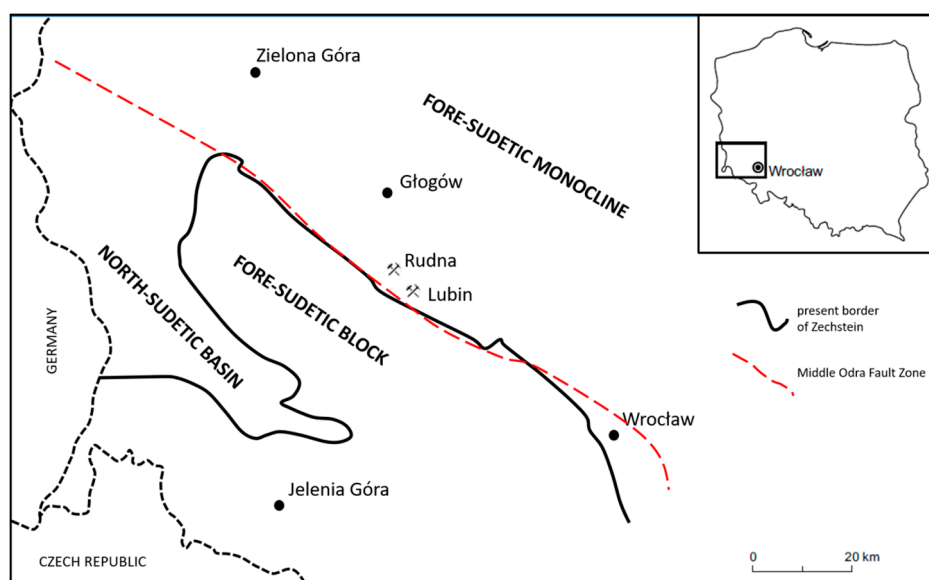

Figure 1. Location of the Fore-Sudetic Monocline against Poland and the mines probed against the main surrounding cities.
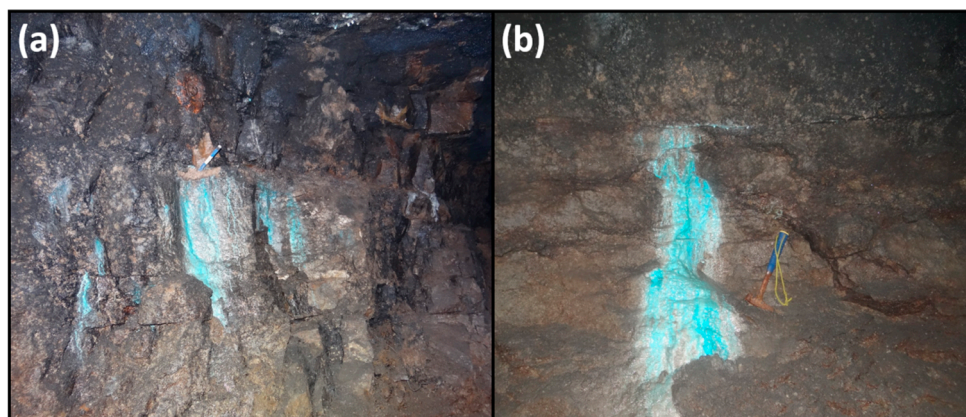
Figure 2. Field images from the Lubin Główny mine collecting site. The white-blue dripstones are seen. Note the hammer for scale. (**a**) General view, (**b**) A close-up view.

The determination of the mineralogical nature of the Cu-bearing samples began with Powder X-Ray Diffraction (PXRD) technique. Powdered sample was placed in a Bruker D8 ADVANCE equipped with superfast linear position-sensitive detector (LPSD) VÅNTEC-1 and kβ-filtered CoKα radiation. The apparatus is located in the Institute of Geological Sciences, Polish Academy of Sciences (Cracow section, Poland). The samples were scanned using $0.02 \, 2\theta$ increment and 1 s/step counting time (equivalent of 416 s in the zero-dimensional detector language), in the $3–80 \, 2\theta$ range. Some additional samples were analyzed using a Thermo Electron X'TRA diffractometer at the same location, using similar conditions but 0.3°/min rate. Unit cell parameters were calculated using the Rietveld method implemented in the TOPAS v. 3.0 software. The macroscopic features of the mineral assemblages and minerals themselves were studied using a camera-equipped binocular. The photo layering (stacking) technique was involved to obtain the best-focused images. The crystal chemistry and spatial relation of the particular minerals were analyzed using electron microprobe (EPMA), using a CAMECA SX100 apparatus operating in the WDS mode and located in the Inter-Institution Laboratory of Microanalysis of Minerals and Synthetic Substances, Institute of Geochemistry, Mineralogy and Petrology, Faculty of Geology, University of Warsaw, Warsaw, Poland. The beam current and size were variable depending on the particular minerals analyzed (see tables for details); the acceleration voltage was 15 kV. Sodium, as a light element prone to fast escape during analyzing, was measured using time-zero intercept method. In this method, the sodium concentration is measured at various steps of the full analysis and then approximated to time of zero. The following standards were used: albite (Na), baryte (S), celestine (Sr), crocoite (Pb), CoO (Co), NiO (Ni), cuprite (Cu), diopside (Mg, Ca, Si), Fe_2O_3 (Fe), GaAs (As), InSb (Sb), orthoclase (Al, K), rhodonite (Mn), sphalerite (Zn), tugtupite (Cl), and YPO_4 (P).

3. Results

3.1. Mineral Composition and Habit

3.1.1. Rudna IX Mine Materials

Both dark dolomite samples and white sandstone samples from the Rudna IX mine are covered by rich accumulations (Figure 3) comprising:

- azurite-like, dark blue, clearly monoclinic crystals, reaching ~2 mm in length;
- dominant in terms of volume, light blue, platy/scaly encrustations, covering areas up to few cm^2, with single plates not larger than ~0.4 mm (usually up to ~0.2 mm);
- medium-green microbotryoidal, compact encrustations surrounding the blue zones;
- white to very pale greenish socket-like, thin, curved linings, up to few centimeters in length.
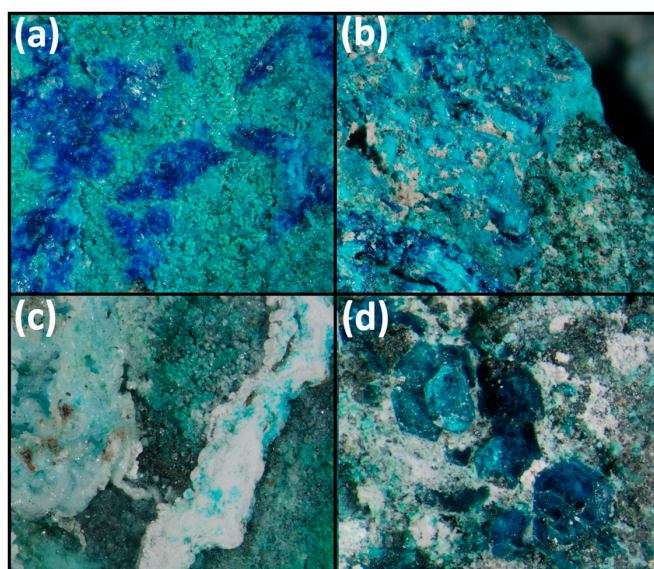
Figure 3. Microphotographic documentation of the Rudna IX mine secondary mineralization under scope. (**a**) Azure-colored chalconatronite crystals with minor light blue replacement juangodoyite and green malachite; (**b**) Juangodoyite-rich portion; (**c**) Aragonite-rich socket-like margin accumulations; (**d**) Second-type dioptase-like chalconatronite crystals; (**a**)–(**c**): 8 mm field of view; (**d**): 3 mm field of view.

The azure crystals are spear-like and commonly intergrown into more or less compact masses that may surpass 4 mm in diameter. In some samples, the interiors of the azure crystals are either partially or completely replaced by the light blue phase. Various stages of chalconatronite replacement are observed (Figure 4).
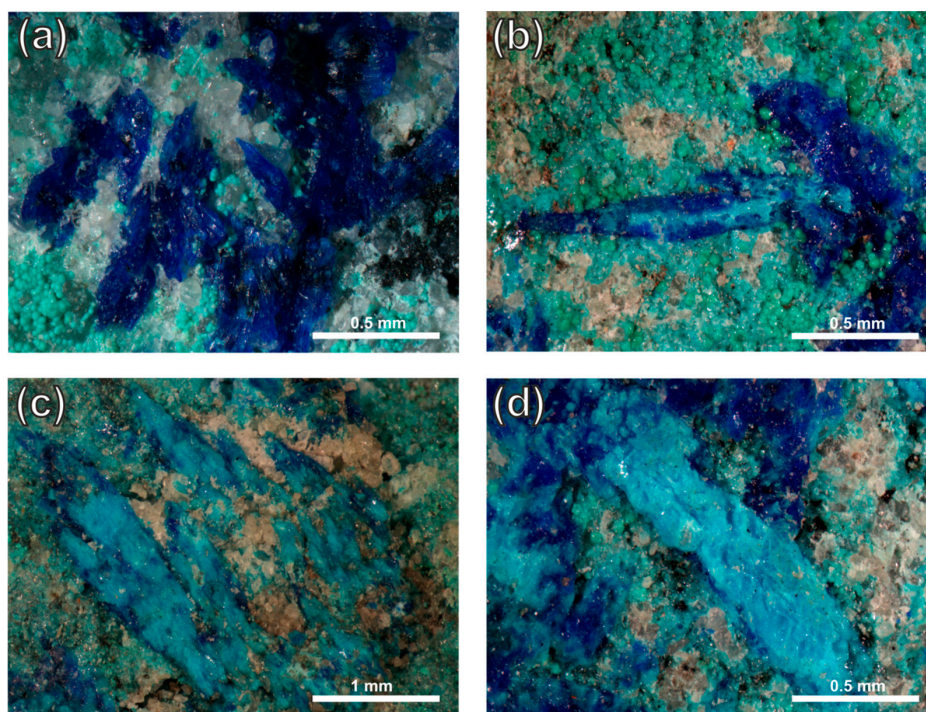
Figure 4. Microphotographic documentation of the chalconatronite-juangodoyite pseudomorphic relation. (**a**) Virtually intact chalconatronite crystals; (**b**) Initial stage of internal juangodoyite replacement; (**c**) Almost completely juangodoyite-replaced chalconatronite crystals; (**d**) Replaced and fresh chalconatronite crystals.

The dark green phase forms aggregates with single botryoids under 0.2 mm in diameter; no individual crystals were observed among them. This phase occurs between and beneath the two blue species (Figure 3a). Rare examples concern the coarse-botryoidal green phase associated with closely-packed azure crystals. The white socket-like aggregates also stand for an important matrix constituent, where they associate with the green phase. Their greenish parts are locally somewhat rounded (cauliflower-like in shape). In a few specimens, these sockets are stained bluish (Figure 3c). Close examination of a side part of a single specimen of dolomite allowed us to pinpoint an additional type of substance that occurs as intergrown pseudotrigonal crystals of teal colour, somewhat resembling dioptase (Figure 3d).

The PXRD analysis of the Rudna IX minerals results are juxtaposed in the Table 1. As some of the samples comprise various types of aggregate, some minerals reported in the above quantitative data may represent random accumulations of particular species. This is especially the case of herbertsmithite, which was not yet detected during the EPMA sessions. The issue addressed reflects the large level of mineralogical variability in the material studied.

The light-blue phase is usually juangodoyite. The dark blue one and the dioptase-like one is chalconatronite. However, at least a single case of the azure crystals (sample CuR4, which also bears orange baryte) were shown by the PXRD to be juangodoyite, too. As such, the precise identification of the mineralogical nature of both phases proves to be complex and blurred by the hydration-dehydration dependence of the two minerals. The green botryoidal mineral is usually malachite. However, the rare, coarser (up to ~0.20 mm) botryoids associated with azure juangodoyite are cornwallite, one of the natural polymorphs of $Cu_5(AsO_4)_2(OH)_4$. This phase may cover areas over 2 mm long.

The white socket-like aggregates are mainly composed of gypsum and aragonite. Hydromagnesite, $Mg_5(CO_3)_4(OH)_2·4H_2O$, and the rare mineral northupite, $Na_3Mg(CO_3)_2Cl$, are present, too. The greenish and bluish parts of the socket-like aggregates are colored by a Cu–Cl–O species—with clinoatacamite and herbertsmithite, respectively. Separate clinoatacamite-dominant zones surrounded by thin halite/gypsum linings on a sandstone matrix (e.g., sample CuR6) may be as large as 2 mm in diameter.

A second batch of two, small samples, representing halite encrustations filled with some further secondary Cu minerals most likely derived from another, currently unknown section of the mine, was also studied in a preliminary manner. These samples bear eriochalcite, $CuCl_2·2H_2O$, ktenasite, $Zn(Cu,Zn)_4(SO_4)_2(OH)_6·6H_2O$, and kröhnkite, $Na_2Cu(SO_4)_2·2H_2O$ (sample RSR9-1); or are kröhnkite-dominant (RSR9-2). A single sample (RSR9-3) of a dolomitic shale covered by compact, light-blue material, proved to bear further interesting species associated with chalconatronite—a lavendulan-group species, with best PXRD fit for likely lavendulan sensu stricto, $NaCaCu_5(AsO_4)_4Cl·5H_2O$. The mixture of the two is covered by spray-forming needle-like aragonite intergrown with hydromagnesite (sample RSR9-4—a sub-sample of the RSR9-3 one). Results of a more detailed study of both these phases and cornwallite, lavendulan-group phase, kröhnkite, and eriochalcite will be published elsewhere.

A number of additional mineral phases were tentatively determined in the course of the whole PXRD data treatment, as reported in the Table 1. State of art allows us to mention those of the uncertain species which are most likely to occur in the material studied considering both the initial PXRD identification and local geochemical conditions. The list is opened by wooldridgeite (samples CuR1, CuR1A, and CuR6), a very unique Na-Cu pyrophosphate which may, however, be coincident with nesquehonite, $MgCO_3·3H_2O$. The latter phase conjures up the identification of chemically related hydromagnesite and northupite. The same is true, e.g., for wegscheiderite, $Na_5H_3(CO_3)_4$ (two other Na carbonates—trona and nahcolite—were, indeed, observed in some additional samples analyzed by E.S.). Possible coexisting Cu minerals include paratacamite, atacamite; melanothallite, Cu_2OCl_2, kipushite, $(Cu,Zn)_5Zn(PO_4)_2(OH)_6·H_2O$, and the langite- and wroewolfeite-related mineral posnjakite, $Cu_4(SO_4)(OH)_6·H_2O$. A likely phase is rhomboclase, $(H_5O_2)Fe(SO_4)_2·2H_2O$, is genetically related to melanterite (e.g., [40]).

Table 1. Results of the PXRD analysis of the samples from the Rudna IX mine.

Sample	Macroscopic Description	Main Components [1]	Rietveld Refinement Statistics [2]
CuR1	azure, light-blue, and green crystals/aggregates on a dolomitic shale	chalconatronite 37.5(2), quartz 36.1(2), illite 9.1(5), malachite 7.7(5), juangodoyite 4.4(3), orthoclase 1.7(3).	R_{wp} = 9.67%, GOF (χ^2) = 1.37%
CuR1A	shiny greenish-blue crystals + matrix, same sample	chalconatronite 62.5(7), illite 23.5(8), microcline 8.1(1), Mg-calcite 1.0(6), clinoatacamite 0.8(3).	R_{wp} = 20.54%, GOF (χ^2) = 2.84%
CuR1B	white to greenish socket-like aggregates, same sample	aragonite 57.2(4), quartz 25.6(3), hydromagnesite 5.9(4), microcline 4.1(3), herbertsmithite 2.7(8), halite 1.9(1), albite 1.8(2), northupite 0.07(4).	R_{wp} = 11.48%, GOF (χ^2) = 0.97%
CuR2A	white sandstone with disseminated green mineral and surface black dendritic specks	quartz 47.1(2), halite 19.4(9), gypsum 8.2(4), clinoatacamite 9.9(7), herbertsmithite 5.3(6), illite 4.1(4), microcline 3.4(6), orthoclase 1.8(4), albite 0.8(5).	R_{wp} = 10.38%, GOF (χ^2) = 1.18%
CuR2B	colorless crystalline cover of the former	halite 90.3(7), gypsum 3.4(3), quartz 3.4(4), clinoatacamite 2.0(4), herbertsmithite 0.9(3).	R_{wp} = 29.42%, GOF (χ^2) = 2.31%
CuR3 [3]	light-blue and minor azure and green aggregates/crystals on a white sandstone	quartz 69.6(7), calcite 9.1(3), chalconatronite 5.0(3), halite 4.3(2), microcline 2.9(5), albite 2.7(5), malachite 2.5(3), orthoclase 1.8(3), juangodoyite 1.2(2), dolomite 0.5(1).	R_{wp} = 18.57%, GOF (χ^2) = 2.02%
CuR3A	separate white accumulations, same sample	quartz 58.9(2), aragonite 17.2(7), gypsum 6.7(3), calcite 3.9(3), dolomite 3.5(3), orthoclase 1.2(2), langite 0.4(1); wroewolfeite, illite (trace).	R_{wp} = 13.69%, GOF (χ^2) = 1.12%
CuR3B	separate white accumulations, same sample	gypsum 61.9(5); quartz 19.6(3), aragonite 10.4(4), monohydrocalcite 3.9(3), baryte 2.8(4), calcite 2.7(3), dolomite 1.5(4).	R_{wp} = 14.86%, GOF (χ^2) = 1.34%
CuR4 [3]	intergrown azure crystals + coarse green botryoids + cellular white infillings in a dolomitic shale	albite 28.7(1), calcite 11.2(2), aragonite 17.7(2), quartz 5.8(8), juangodoyite 5.5(7), cornwallite 4.4(6), chalcocite 2.0(9).	R_{wp} = 12.98%, GOF (χ^2) = 1.93%
CuR6	similar to CuR2 but with black material replaced by a limonite-like one	quartz 58.2(7), halite 15.2(6), herbertsmithite 9.1(2), gypsum 5.3(2), microcline 7.0(6), orthoclase 1.8(4), albite 3.5(4).	R_{wp} = 14.01%, GOF (χ^2) = 1.26%
RSR9-1	small rounded bluish-green aggregates	eriochalcite 38.7(1), halite 36.7(1), ktenasite 12.4(4), kröhnkite 9.7(1), chlorite group 2.4(1).	R_{wp} = 29.75%, GOF (χ^2) = 2.83%
RSR9-2	small bluish-green crust	kröhnkite 86.2(2), halite 8.2(2), gypsum 2.6(3).	R_{wp} = 11.23%, GOF (χ^2) = 0.96%
RSR9-3	light to medium-blue compact masses on a dolomitic shale	chalconatronite 54.7(7), clinoatacamite 2.9(3), albite 5.1(4), eriochalcite 3.2(5), lavendulan group 1.8(1).	R_{wp} = 22.60%, GOF (χ^2) = 1.76%
RSR9-4	white spray-forming needles covering the above	aragonite 73.2(5), hydromagnesite 13.4(5), melanterite 7.7(2), lavendulan group 3.1(1), quartz 2.7(2).	R_{wp} = 15.63%, GOF (χ^2) = 0.75%

[1] wt.% contents reported based on Rietveld quantitative phase analysis (QPA); slight deficiency is due to initial inclusion of minor and/or uncertain species in the refinements (see main text for details); [2] for QPA model; [3] a mixed sample (various types of aggregates).

3.1.2. Lubin Główny Minerals

The microphotographs of the Lubin Główny paragenesis are juxtaposed in Figure 4. The Lubin Główny paragenesis is much less complex than the former one (Table 2).

Table 2. Results of the PXRD analysis of the Lubin Główny mine secondary minerals.

Sample	Macroscopic Description	Main Components [1]	Rietveld Refinement Statistics [2]
MSCu-1 [3]	thin light blue crusts (A) with white/beige/gray protrusions (B), all on a white-pinkish sandstone	aragonite 40.4(4), quartz 20.9(3), gypsum 19.4(3), calcite 7.6(4), monohydrocalcite 7.2(2), vaterite 1.5(4), dolomite 1.2(2)	R_{wp} = 13.53%, GOF (χ^2) = 1.10%
Cu4 [3]	thick greenish-blue dripstones (A) covered by gray/white protrusions (B) and colourless sprays (C)	dolomite 30.2(5), monohydrocalcite 15.5(4), aragonite 14.4(5), rapidcreekite 11.2(4), gypsum 7.6(4), quartz 7.4(3), calcite 6.8(3), vaterite 5.2(6)	R_{wp} = 16.97%, GOF (χ^2) = 1.53%

[1] wt.% contents reported based on Rietveld quantitative phase analysis (QPA); slight deficiency is due to initial inclusion of minor and/or uncertain species in the refinements (see main text for details); [2] for the QPA model; [3] a mixed sample (various types of aggregates).

As opposed to prior suggestions (e.g., [38]), the blue coloration of the thin encrustations (sample MSCu-1, Figure 5a) does not come from geminite, $Cu(AsO_3OH) \cdot H_2O$. Instead, these aggregates are composed of monohydrocalcite, aragonite, gypsum, quartz, and minor calcite. Vaterite and dolomite are trace species here. The gray protrusions are mainly comprising gypsum. The sample Cu4 (Figure 5b) also bears sprays—up to ~2.4 mm in diameter—composed of colorless needles of rapidcreekite. Single needles are up to 1 mm long. Such spray-forming needle-like crystals of rapidcreekite were also mentioned in [38]. The coloring agent is mainly a not yet fully analyzed CuZnNiCoCa(MnMg) arsenate. Brushite, $Ca(PO_3OH) \cdot 2H_2O$, although suggested by the Rietveld method to be present at ~2 wt.% level, could not be found in the material separated for the EPMA study. A very small P impurity was only detected in a few EDS spectra of gypsum. The thick, blue to greenish-blue, bulky encrustations (sample Cu4) are also composed of aragonite, with gypsum, calcite, dolomite, and monohydrocalcite as coexisting or trace components. The identification of moolooite, $Cu[(COO)_2]_2 \cdot 0.4H_2O$, needs further examination.
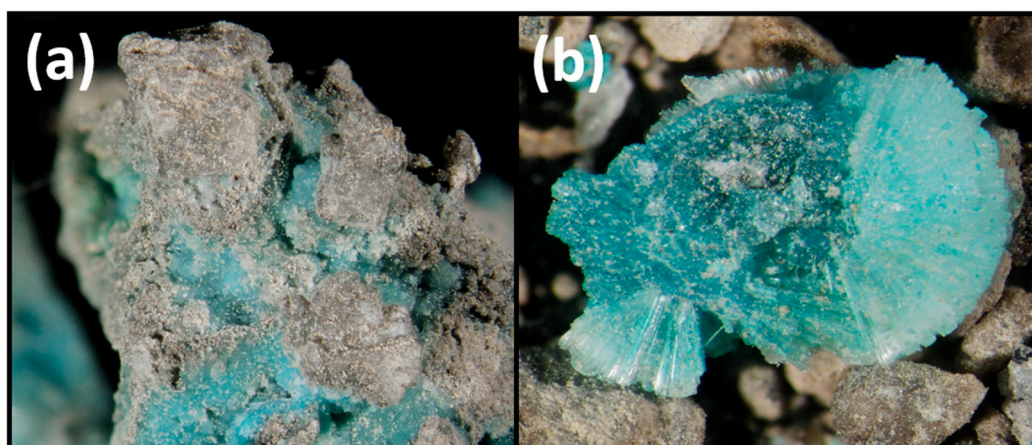

Figure 5. Microphotographic documentation of the Lubin Główny mine secondary mineralization under scope. (**a**) Thin monohydrocalcite- and aragonite-rich encrustations with gypsum-rich grey protrusions; field of view is 8 mm; (**b**) Rapidcreekite needle-bearing sprays covering thick Ca-carbonate encrustations; field of view is 4 mm.

3.2. Spatial Relations, Crystal Chemistry and Unit Cell Parameters of the Minerals

The BSE images of both locality samples are juxtaposed in Figure 6. Both juangodoyite and chalconatronite bear malachite and chalcocite inclusions (Figure 6a,b). Aragonite and quartz may be included in chalconatronite (Figure 6b). Malachite either occurrs as usually rounded to botryoidal, small inclusions, or larger, rounded, spherolitic aggregates are found outside the Na-Cu carbonates. The botryoids may reach 50 μm in diameter. Malachite may be interstitial (Figure 6a–c). Still larger, elongated malachite aggregates, reaching ~250 μm in length, were also observed. The socket-forming aragonite is a core species, overgrown by hydromagnesite and northupite (Figure 6d). The northupite and hydromagnesite zones alone can be as large as 200 μm in width, with aragonite cores >400 μm in diameter.
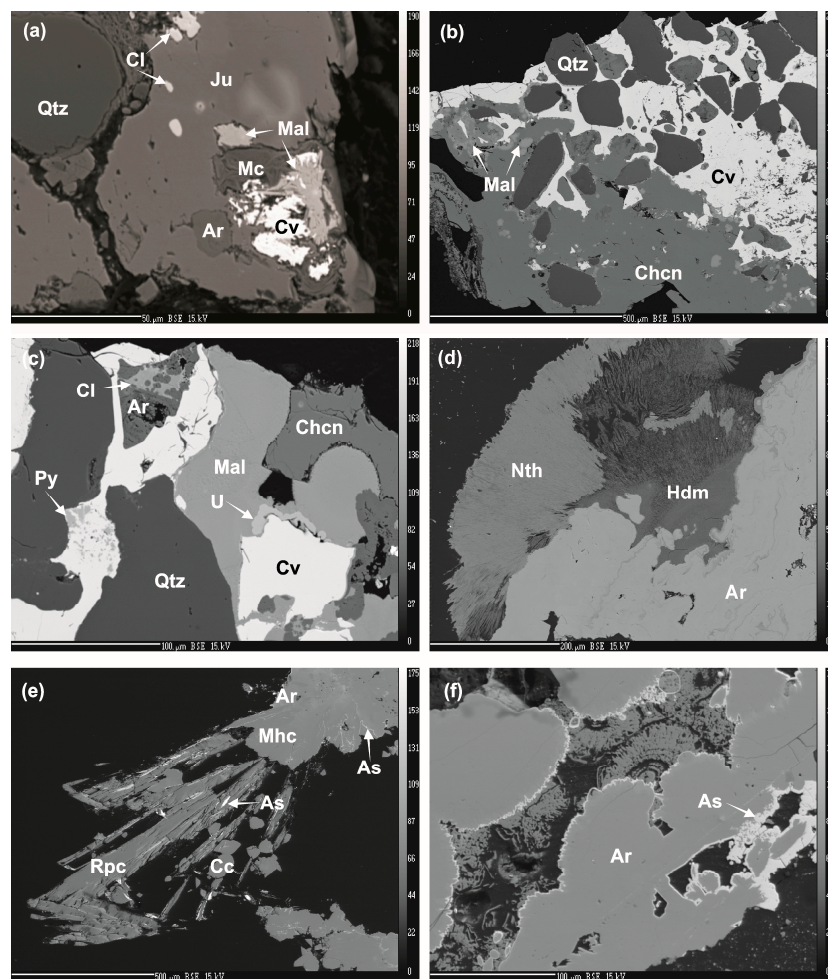
Figure 6. BSE (Back-Scattered Electron) images from electron microprobe (EPMA) analytical sessions of Rudna IX mine (panels a–d) and Lubin Główny mine (panels e & f) mineral assemblages. (**a**) Juangodoyite (Ju) crystals among quartz (Qtz) with included clinoatacamite (Cl), covellite (Cv), malachite (Mal), and Cu-bearing mica-like phase (Mc); (**b**) Large chalconatronite (Chcn) crystal (azure-blue in normal light) with malachite inclusions, quartz, and covellite; (**c**) Enlarged view of a fragment of "(b)" aggregate showing pyrite (Py) inclusions in covellite and a Cu–Cl–O phase (Cl) included in aragonite (Ar); U—unnamed Cu-rich phase (see analysis no. 12 in Table 5); (**d**) A fragment of white socket-like aggregate with aragonitic core overgrown by hydromagnesite (Hdm) and northupite(Nth)-bearing mixture; (**e**) Large spray-forming crystals of rapidcreekite (Rpc) growing on aragonite/monohydrocalcite (Ar/Mhc) with very thin ribbons of CuZnNiCoCa(MnMg) arsenate (As); calcite (Cc) crystals also visible; (**f**) Dolomite-rich sample overgrown by aragonite dripstone covered by the mentioned arsenate (As).

3.2.1. The Rudna IX Minerals Data

Juangodoyite and chalconatronite are chemically very pure and have very similar empirical formulas. The crystal chemistry of the light blue phase, juangodoyite (Table 3), is described as $Na_{2.41}Cu_{1.00}(CO_3)_{2.21}$ ($n = 7$, i.e., first aggregate). The corresponding formula for a second aggregate ($n = 3$) is $Na_{2.55}Cu_{1.00}(CO_3)_{2.28}$. The two formulas bear average 0.48 surplus Na, in spite of the use of the time-zero intercept measurement method. After the stoichiometric normalization of wt.% Na_2O content to the ideal content, the formulas take the form of $Na_{2.00}Cu_{1.00}(CO_3)_{2.00} \cdot 3H_2O$. Chalconatronite analyses are juxtaposed in Table 4. The corresponding formula for the azure, spear-like crystals of chalconatronite is $Na_{2.00}Cu_{1.00}(CO_3)_{2.00}$ ($n = 10$; anhydrous part due to almost complete dehydration due to beam energy) after the normalization of wt.% Na_2O to the ideal composition of the species. Un-normalized analysis gives mean 0.33 *apfu* Na excess. The analysis of two greenish-blue dioptase-like crystals of chalconatronite gave the following empirical formula (using 3-cation-basis, i.e., $\Sigma(Na,Cu) = 3$, recasting basis): $Na_{1.93–1.96}Cu_{1.07–1.04}[(CO_3)_{2.03–2.00}(SiO_3)_{0.01–0.02}]_{\Sigma 2.04–2.02}$ (anhydrous basis due to mineral destruction). Similar wt.% data for juangodoyite and chalconatronite have two sources: (1) the dehydration of chalconatronite under the electron beam, leading to an equivalent of juangodoyite, and (2) pseudomorphic relation of the two species, constricting macroscopic species distinction. The deviation of the listed wt.% data from comparative data of the Handbook of Mineralogy is, again, due to mineral's instability in the microprobe column.

Table 3. Results of the EPMA analyses of the Rudna IX mine juangodoyite (sample CuR1A, crystal 1: analyses 1–7; crystal 2: analyses 8–10).

Analysis no.:	1	2	3	4	5	6	7	8	9	10	11 [1]
					wt.% [2]						
CuO	33.12	32.43	33.80	33.18	32.87	33.31	32.91	33.63	33.86	32.80	33.77
Na_2O	29.18	30.46	30.42	29.04	33.38	31.89	32.65	33.44	33.88	32.35	28.27
Total-1	62.30	62.88	64.23	62.22	66.26	65.20	65.55	67.08	67.75	65.15	
CO_2 [3]	36.65	35.88	37.41	36.71	36.38	36.86	36.41	37.22	37.47	36.30	38.45
Total-2	98.95	98.77	101.63	98.93	102.63	102.06	101.97	104.30	105.22	101.45	100.49
					apfu [1 Cu cation basis]						
Cu	1.00	1.00	1.00	1.00	1.00	1.00	1.00	1.00	1.00	1.00	
Na	2.26	2.41	2.31	2.25	2.61	2.46	2.55	2.55	2.57	2.53	
Na_N [4]	2.00	2.00	2.00	2.00	2.00	2.00	2.00	2.00	2.00	2.00	
$(CO_3{}^{2-})$ [4]	2.00	2.00	2.00	2.00	2.00	2.00	2.00	2.00	2.00	2.00	
beam amperage [nA]	10	10	10	10	10	10	10	10	10	10	
spot size [μm]	10	10	10	10	10	10	10	10	10	10	

			Unit Cell Parameters			
sample	*a* [Å]	*b* [Å]	*c* [Å]	β [°]	R_{wp} [%]	GOF [%]
CuR1	6.170(1)	8.177(4)	5.565(4)	116.20(4)	8.11	1.21
CuR3	6.110(8)	8.10(1)	5.655(3)	116.47(11)	17.09	2.14
CuR4	6.110(9)	8.25(2)	5.618(5)	116.23(12)	10.54	1.65

[1] comparative composition from [41], Santa Rosa mine material; [2] S, Si, Al, Fe, Mn, Zn, Mg, Ca, Sr, and K were analyzed but not detected; [3] backward calculation with wt.% derived from stoichiometrically calculated, charge-balance amount of $CO_3{}^{2-}$; [4] occupancy-normalized and ideal amount.

Table 4. Results of the EPMA analyses of the Rudna IX mine chalconatronite (sample CuR4).

Analysis no.:	1	2	3	4	5	6	7	8	9	10 [1]	11 [1]	12 [2]
wt.% [3]												
SiO_2	0.00	0.00	0.00	0.00	0.00	0.00	0.00	0.00	0.00	0.24	0.48	
CuO	33.51	33.03	34.19	33.72	32.61	33.39	33.89	32.55	32.75	36.59	38.97	29.2
CaO	0.18	0.22	0.00	0.25	0.27	0.00	0.00	0.00	0.21	0.00	0.00	
Na_2O	30.49	30.23	31.89	31.63	29.72	30.27	29.27	30.83	29.43	25.76	28.75	19.7
Total-1	64.60	63.48	66.08	65.61	62.60	63.65	63.16	63.41	62.39	62.59	68.20	
CO_2 [4]	37.85	36.89	37.83	37.71	36.51	36.94	37.50	36.07	36.56	38.36	41.62	30.5
H_2O [5]					0.89			0.52	1.05			19.0
Total-2	102.24	100.37	103.91	103.32	99.11	100.60	100.66	99.48	98.95	100.95	109.82	99.4
apfu [Σ(Cu,Ca,Mg) = 1 basis (analyses 1–9); 3 cations (analyses 10 & 11)]												
Si										0.01	0.02	
Cu	0.98	0.99	1.00	0.99	0.99	1.00	1.00	1.00	0.99	1.07	1.04	
Mg	0.01											
Ca	0.01	0.01		0.01	0.01				0.01			
Na	2.29	2.33	2.39	2.38	2.31	2.33	2.22	2.43	2.29	1.93	1.96	
Na_N [6]	2.00	2.00	2.00	2.00	2.00	2.00	2.00	2.00	2.00	2.00	2.00	
(CO_3^{2-}) [6]	2.00	2.00	2.00	2.00	2.00	2.00	2.00	2.00	2.00	2.00	2.00	
beam amperage (nA)	10	10	10	5	10	10	10	10	10	10	10	
spot size (μm)	10	10	10	10	10	10	10	10	10	10	10	
Unit Cell Parameters												

sample	a [Å]	b [Å]	c [Å]	β [°]	R_{wp} [%]	GOF [%]
CuR1	9.694(1)	6.0937(7)	13.7845(1)	91.902(8)	8.11	1.21
CuR3	9.61(1)	6.099(5)	13.788(6)	91.77(7)	17.09	2.14
RSR9-3	9.686(2)	6.096(2)	13.786(3)	91.88(21)	19.53	1.48

[1] Two analyses of dioptase-like crystals from side part of the sample; [2] comparative composition from [41], Egyptian patina material; [3] S, Al, Fe, Mn, Zn, Mg, Sr, and K were analyzed but not detected; [4] backward calculation from amount of CO_3^{2-} set as ideal content; [5] by difference (100-Total1-wt.% CO_2); [6] occupancy-normalized and ideal amount.

The Na-Cu carbonates are closely associated with slightly magnesian malachite (Table 5). Large chalconatronite crystals were observed to be intergrown with quartz (which may include the latter) and bearing inclusions of chalcocite ("type 1", Figure 6b). Some chalcocites bear numerous, tiny inclusions of chemically pure pyrite or marcasite. Chalcocite may also enclose strontian aragonite with single inclusions of a Cu–O–Cl phase (non-analytical). Malachite is either found to be directly overgrowing chalconatronite, including it, or residing between quartz and chalcocite inclusions in chalconatronite (Figure 6c). The first type bears less Mg (analyses 1–5, Table 5); its empirical formula based on a larger analytical representation (n = 9) is $(Cu_{1.92}Mg_{0.04}Na_{0.04})_{\Sigma2.00}(CO_3)_{1.00}(OH)_{1.96}$. This, when omitting Na, corresponds to the mean end-member representation of $Mal_{98}Mgc_2$ where Mal stands for malachite and Mgc for mcguinnessite. Second-type malachite, forming much larger, ovoid-shaped but also typical, rounded aggregates ("type 2", Figure 6b), is more magnesian: $(Cu_{1.85}Mg_{0.10}Na_{0.05})_{\Sigma2.00}(CO_3)_{1.00}(OH)_{1.95}$. This formula corresponds to normalized (Na-devoid) representation of $Mal_{95}Mgc_5$. An additional, very minor phase was observed as thin (up to ca. 9 μm thick and ca. 45 μm in length), lobate, curved accumulation at a malachite-chalcocite interface (Figure 6c, phase "U"). Only a single analysis could be obtained. Its chemical composition (analysis no. 12 in Table 5) does not fit to any known mineral species.

Table 5. Results of representative EPMA analyses of the Rudna IX mine malachite (sample CuR4; analyses 1–11) and an unnamed inclusion phase (analysis 12).

Analysis no.:	1 [1]	2	3	4	5	6	7	8	9	10	11	12
					wt.% [2]							
SO_3	0.00	0.00	0.00	0.00	0.00	0.00	0.00	0.21	0.00	0.00	0.00	0.00
SiO_2	0.00	0.00	0.00	0.00	0.00	0.00	0.00	0.00	0.00	0.00	0.00	1.71
FeO	0.00	0.00	0.00	0.00	0.00	0.00	0.07	0.00	0.00	0.00	0.00	0.88
CuO	67.34	67.02	67.72	70.04	66.34	67.92	65.01	66.48	68.08	67.17	67.31	81.86
MgO	0.76	0.70	0.35	0.87	0.38	2.23	2.40	2.05	2.03	1.50	1.57	0.00
CaO	0.00	0.00	0.00	0.00	0.00	0.00	0.00	0.00	0.00	0.00	0.00	0.10
Na_2O	0.50	0.63	0.63	0.52	0.25	0.80	0.79	0.69	0.63	0.59	0.68	0.00
Total-1	68.60	68.38	68.69	71.42	66.98	70.95	68.26	69.43	70.73	69.29	69.55	84.45
CO_2 [3]	19.04	18.93	18.92	19.85	18.56	20.01	19.31	19.51	19.94	19.40	19.48	
H_2O [4]	12.36	12.69	12.38	8.73	14.46	9.04	12.42	11.06	9.33	11.34	10.97	
Total-2	100.00	100.00	100.00	100.00	100.00	100.00	100.00	100.00	100.00	100.00	100.00	
					apfu [2 cations basis]							
SO_4^{2-}								0.01				
Cu	1.92	1.91	1.93	1.92	1.96	1.83	1.81	1.84	1.85	1.87	1.87	
Mg	0.04	0.04	0.02	0.05	0.02	0.12	0.14	0.11	0.11	0.08	0.09	
Na	0.04	0.05	0.05	0.04	0.02	0.06	0.06	0.05	0.04	0.04	0.05	
(CO_3^{2-}) [5]	1.00	1.00	1.00	1.00	1.00	1.00	1.00	0.99	1.00	1.00	1.00	
(OH^-) [6]	1.96	1.95	1.95	1.98	1.98	1.96	1.96	1.95	1.96	1.97	1.99	
					End-Members [%] [7]							
Mal	98	98	99	97	99	93	93	94	94	95	94	
Mcg	2	2	1	3	1	7	7	6	6	5	6	
beam amperage (nA)	10	10	10	10	10	10	10	10	10	10	10	10
spot size (µm)	5	5	5	5	5	5	5	5	5	5	5	5

		Unit Cell Parameters				
sample	a [Å]	b [Å]	c [Å]	β [º]	R_{wp} [%]	GOF [%]
CuR1	9.499(3)	11.952(2)	3.243(1)	98.72(4)	8.11	1.21
CuR3	9.50(2)	11.95(2)	3.238(4)	98.61(1)	17.09	2.14

[1] Analyses 1–5: low-Mg variety; analyses 6–11: higher-Mg variety (analyses 6–8 and 9–11 for two separate aggregates); [2] Al, Mn, Zn, and K were analyzed but not detected; [3] backward calculation from amount of CO_3^{2-} set as ideal content; [4] by difference (100-Total1-wt.% CO_2); [5] occupancy-normalized amounts; [6] by charge balance; [7] normalized to Cu- and Mg-dominant end-members only.

A very interesting, though relatively subordinate, Cu-bearing K-Na-Ca-Mg(Fe) aluminosilicate phase is occasionally found as an inclusion in juangodoyite (Figure 6a). The results of the EPMA analyses of this phase are reported in Table 6. This phase is somewhat reminiscent of the Cu-bearing glauconite of [42] which, however, has >7 wt.% MgO, >6 wt.% Na_2O, and just up to 2.02 wt.% CuO. Recasting the first analysis to muscovite stoichiometry gives the empirical formula of $(K_{0.67}Cu_{0.30}Ca_{0.03})_{\Sigma1.00}(Al_{1.57}Mg_{0.26}Cu_{0.10}Fe_{0.07})_{\Sigma2.00}(Al_{0.42}Si_{3.58}O_{10})[(OH)_{1.45}O_{0.55}]_{\Sigma2.00}$, assuming trivalent Fe. The second analysis listed gives the $(K_{0.61}Cu_{0.16}Na_{0.15}Ca_{0.06})_{\Sigma0.98}(Al_{1.56}Mg_{0.26}Cu_{0.15}Fe_{0.03})_{\Sigma2.01}(Al_{0.51}Si_{3.49}O_{10})[O_{1.30}(OH)_{0.62}S_{0.08}]_{\Sigma2.00}$ formula. The X site occupancy in both cases is calculated by stoichiometry, charge balance, and according to the current nomenclature of the mica group. The second analysis fits to the Al-dominant analogue of oxyphlogopite—a potentially new mineral. This mineral is, however, another case needing further study to confirm its suggested mica-group membership, site occupancy and Cu and Fe valency. This mica-like mineral shows somewhat phengitic or aluminoceladonite-like composition; indeed, [43] also described a Cu-bearing phengite from the Monocline area, suggesting ideal composition of $\sim K_2Mg_2AlCu^{2+}(Fe^{3+}AlSi_6O_{20})(OH)_4$. However, our species do not recast to such stoichiometry.

Table 6. Results of the EPMA analyses of the Rudna IX Cu-bearing aluminosilicates.

Analysis no.:	1 [1]	2	3	4
SO_3	0.00	1.45	0.26	0.00
SiO_2	51.33	50.29	15.29	31.25
TiO_2	n.a. [2]	0.00	0.00	0.00
Al_2O_3	24.41	25.35	7.08	13.93
FeO	1.15	0.60	0.00	0.00
MnO	0.00	0.00	0.00	0.00
CuO	7.65	5.98	4.58	7.31
ZnO	0.00	0.00	0.00	0.00
MgO	2.49	2.49	0.71	1.45
CaO	0.41	0.82	33.60	15.65
Na_2O	0.00	1.14	0.31	0.42
SrO	0.00	0.00	0.00	0.00
K_2O	7.57	6.94	1.78	3.82
Total-1	94.81	95.06	63.62	73.84
H_2O [3]	5.19	4.94	36.39	26.16
Total-2	100.00	100.00	100.00	100.00
apfu (7 cations basis)				
Si	3.58	3.49		
Al	1.99	2.07		
Fe^{3+}	0.07	0.03		
Cu	0.40	0.31		
Mg	0.26	0.26		
Ca	0.03	0.06		
Na		0.15		
K	0.67	0.61		
OH^-	1.45	0.62		
O^{2-}	0.55	1.30		
S^{2-}	0.55	0.08		
^{VI}Al	1.57	1.56		
^{IV}Al	0.42	0.51		
beam amperage (nA)	10	10	10	10
spot size (μm)	5	5	5	5

[1] analyses 1 & 2: a Cu-mica-like material; analyses 3 & 4—a Ca-rich Cu-bearing aluminosilicate; [2] not analyzed; [3] by difference.

Another interesting element of the Rudna IX samples are white aggregates of carbonate minerals. Their cores are made of strontian aragonite, $(Ca_{0.95}Na_{0.03}Mg_{0.02}Sr_{0.01})_{\Sigma1.01}(CO_3)_{1.00}$ ($n = 5$; Table 7) corresponding to $Arg_{95}Ntr_3Srt_1Mgs_1$ where Arg is aragonite, Str is strontianite, Mgs is magnesite end-members, and Ntr is natrite (Na_2CO_3) equivalent.

The occurrence of Na admixture in the aragonite seems somewhat aberrant, but the areas and aragonite individuals analyzed are large and devoid of visible inclusions. Also, Na^+ distribution in calcites and aragonites is mentioned by [44]. Some separate, relatively large grains of core-forming aragonite (Figure 6d) are locally intergrown with BSE-dark phase—hydromagnesite, $Mg_5(CO_3)_4(OH)_2·4H_2O$—and a medium-dark external (rim-forming) phase of a composition suggesting northupite, $Na_3Mg(CO_3)_2Cl$. The latter is probably a mixture or northupite and magnesite. The crystal chemistry of hydromagnesite ($n = 3$, derived from data in Table 8) may be expressed as $(Mg_{4.90}Cu_{0.08}Ca_{0.02})_{\Sigma5.00}(CO_3)_{4.00}(OH)_{2.00}·4.80H_2O$. This leads to 98% of the hydromagnesite member content, the remainder being attributed to unknown Cu- and Ca-dominant analogues.

Table 7. Results of the EPMA analyses of the Rudna IX strontian aragonite (CuR1B sample).

Analysis no.:	1	2	3	4	5
wt.% [1]					
SO_3	0.26	0.34	0.44	0.46	0.00
MgO	0.85	0.00	0.00	0.00	0.56
CaO	52.45	53.96	53.65	54.08	52.71
SrO	1.12	0.84	0.90	0.84	0.96
Na_2O	1.50	0.67	0.64	0.79	1.34
Total-1	56.17	55.81	55.63	56.17	55.58
CO_2 [2]	44.70	43.66	43.40	43.91	44.30
Total-2	100.87	99.47	99.02	100.08	99.87
apfu [1 cation basis]					
$SO_4{}^{2-}$			0.01	0.01	
Mg	0.02				0.01
Ca	0.92	0.97	0.97	0.97	0.93
Sr	0.01	0.01	0.01	0.01	0.01
Na	0.05	0.02	0.02	0.03	0.04
$(CO_3{}^{2-})$ [3]	1.00	1.00	0.99	0.99	1.00
End-Members [%] [4]					
Ar	92	97	97	97	93
Mgs	2				1
Str	1	1	1	1	1
Ntr	5	2	2	3	4
beam amperage (nA)	3	3	3	3	3
spot size (µm)	15	15	15	15	15
Unit Cell Parameters					
sample	a [Å]	b [Å]	c [Å]	R_{wp}	GOF
CuR1b	4.9645(4)	7.9692(7)	5.7542(4)	11.79	1.04
CuR3b	4.963(1)	7.974(3)	5.760(1)	17.75	1.35
CuR4	5.00(1)	8.08(3)	5.80(2)	10.54	1.65
RSR9-4	4.9610(5)	7.9788(8)	5.7611(8)	14.34	0.68

[1] Si, Ti, Al, Fe, Mn, Cu, Zn, and K were analyzed but not detected; [2] backward calculation from amount of $CO_3{}^{2-}$ set as ideal content; [3] occupancy-normalized ideal amounts; [4] see main text for details.

The water content deviation from the ideal content may be related to both material destruction under the electron beam and the porous nature of the aggregates. The latter is also confirmed by analyses no. 4–6 in the same table, with *apfu* data calculated the same way as for hydromagnesite. The identity of the phase related to the latter three analyses is, however, unclear, especially as no higher-hydrate counterparts of hydromagnesite, like giorgiosite, were found in course of the PXRD analysis.

The following ratios were calculated and compared for the northupite-like substance under study (*n* = 8; Table 9) and northupite data from [41]: $Na_2O/(Mg,Cu,Ca)O$, metal oxides/$(CO_2 + SO_3)$, metal oxides/Cl, and Cl/$(CO_2 + SO_3)$. The corresponding values are 1.09, 1.42, 4.97, and 0.29; 2.30, 1.50, 3.76, and 0.40, respectively. After excluding the first analysis used for the correct beam set, recasting the remaining analyses (nos. 2–8) with factor based on five cations gives the empirical formula of $Na_{3.06}(Mg_{1.87}Cu_{0.05}Ca_{0.02})_{\Sigma 1.94}[(CO_3)_{2.90}(SO_4)_{0.02}]_{\Sigma 2.92}Cl_{1.06}$ which may later be burst to $Na_{3.06}(Mg_{0.79}Cu_{0.05}Ca_{0.02})_{\Sigma 0.86}[(CO_3)_{1.82}(SO_4)_{0.02}]_{\Sigma 1.84}Cl_{1.06} + Mg_{1.08}(CO_3)_{1.08}$. The latter procedure is preceded by the calculation of the positive charge, the subtraction of the Cl^- charge, the balancing of the M^{2+} site to occupancy of 1.00 (1 − *apfu*(Cu) − *apfu*(Ca) = $Mg_{northupite}$), the balancing of the remaining charge by the $CO_3{}^{2-}$ groups, and finally relocating the remaining $CO_3{}^{2-}$ and Mg^{2+} to $MgCO_3$. This is equal to Mg distribution derived from ideal Na/M ratio for northupite, calculated by proportion. The carbonate ion inclusion in the above formulas is argued by close association with aragonite. The only

other anion that could exist in place and would explain large wt.% deficiency is OH^-, which is unlikely (Na-Mg-OH-Cl phase is unknown). Halite is also unlikely to exists as a part of the mixture studied due to non-congruent Na/Cl ratio. The northupite-related analyses were also recast with one (Mg + Cu + Ca) cation basis, which does not give good results. The final, normalized empirical formula of northupite is $Na_{3.06}(Mg_{0.93}Cu_{0.05}Ca_{0.02})_{\Sigma1.00}[(CO_3)_{1.97}(SO_4)_{0.02}]_{\Sigma1.99}Cl_{1.06}$, with an average northupite end-member representation of 93%.

Table 8. Results of the EPMA analyses of the Rudna IX hydromagnesite (analyses 1–3) and a related species (CuR1B sample).

Analysis no.:	1	2	3	4	5	6
wt.% [1]						
CuO	1.13	1.29	1.54	0.00	0.00	0.90
MgO	40.53	40.84	40.71	30.64	24.65	29.17
CaO	0.15	0.23	0.27	0.16	0.00	0.18
Total-1	41.81	42.36	42.52	30.79	24.65	30.25
CO_2 [2]	36.00	36.39	36.41	26.86	21.53	25.99
H_2O [3]	22.19	21.25	21.07	42.35	53.81	43.76
Total-2	100.00	100.00	100.00	100.00	100.00	100.00
apfu or mpfu [5 cations basis]						
Mg	4.92	4.90	4.88			
Cu	0.07	0.08	0.09			
Ca	0.01	0.02	0.02			
(CO_3^{2-}) [4]	4.00	4.00	4.00			
(OH^-) [4]	2.00	2.00	2.00			
(H_2O) [5]	5.02	4.71	4.66			
Mg-dominant member content (%)	98	98	98	98	100	98
beam amperage (nA)	3	3	3	3	3	3
spot size (μm)	15	15	15	15	15	15
Unit Cell Parameters						
sample	a [Å]	b [Å]	c [Å]	β [°]	R_{wp}	GOF
CuR1B	10.10(3)	8.947(9)	8.372(9)	114.54(25)	11.79	1.04

[1] S, Al, Fe, Mn, Zn, Sr, Na, K, and Cl were analyzed but not detected; [2] backward calculation from amount of CO_3^{2-} set as ideal one; [3] calculated after backward wt.% CO_2 calculation, as wt.% H_2O = 100-total-(wt.% CO_2); [4] occupancy-normalized ideal amounts; [5] by difference, after subtracting *apfu*(H) attributed to OH^-.

The generally white accumulations are locally greenish due to inclusions of either single microcrystals or veinlets of a Cu–Cl–O phase. According to the PXRD data, this phase is represented by herbertsmithite (or an isostructural substance). However, no Zn- or Mg-bearing Cu–Cl–O species were found in the material portions selected for the EPMA study. Instead, the EPMA analyses (Table 10) recast to clinoatacamite stoichiometry, which is in compliance to the PXRD data for other portions of the material. The recasted EPMA data, indeed, give the OH:Cl ratio of 2.99:0.99. Clinoatacamites analysed in two separate samples, CuR1B and CuR3, are chemically very similar and their chemistry may be expressed as $(Cu_{1.95}Mg_{0.05})_{\Sigma2.00}(OH)_{3.00}Cl_{1.00}$ (n = 11), and $(Cu_{1.97}Mg_{0.03})_{\Sigma2.00}(OH)_{3.03}Cl_{0.97}$ (n = 6), respectively. The formulas suggest a respective 2% and 1% mean part of "anhydrous korshunovskite counterpart", $Mg_2(OH)_3Cl$.

Table 9. Results of the EPMA analyses of the Rudna IX northupite-like species (CuR1B sample).

Analysis no.:	1	2	3	4	5	6	7	8	9 [1]
					wt.% [2]				
SO_3	0.38	0.50	0.49	0.45	0.43	0.42	0.41	0.46	0.08
CuO	1.25	1.17	1.09	1.25	1.05	1.05	1.11	1.05	
MgO	28.08	23.27	21.59	21.41	22.28	24.59	21.00	23.79	16.08
CaO	0.37	0.35	0.27	0.16	0.19	0.72	0.48	0.38	
Na_2O	25.02	29.23	28.94	30.95	29.14	25.29	28.91	26.77	36.99
Cl	9.57	11.92	11.13	11.24	11.67	11.79	12.04	11.49	14.10
Total-1	64.66	66.44	63.51	65.45	64.75	63.86	63.94	63.94	
CO_2 [3]	43.25	39.37	38.01	38.94	38.26	38.41	36.75	38.48	35.12
Total-2	107.91	105.81	101.52	104.39	103.01	102.27	100.69	102.42	
				apfu [5 cations basis]					
SO_4^{2-}	0.02	0.02	0.02	0.02	0.02	0.02	0.02	0.02	
Cu	0.05	0.05	0.05	0.05	0.04	0.05	0.05	0.04	
Mg	2.28	1.87	1.80	1.72	1.83	2.10	1.76	2.00	
Ca	0.02	0.02	0.02	0.01	0.01	0.04	0.03	0.02	
Na	2.64	3.06	3.14	3.22	3.11	2.81	3.16	2.93	
Cl	0.88	1.09	1.05	1.02	1.09	1.14	1.15	1.10	
$CO_3^{2-}{}_{(tot)}$ [4]	3.22	2.90	2.88	2.86	2.88	3.00	2.83	2.97	
$CO_3^{2-}{}_{(northupite)}$ [4]	1.74	0.92	2.06	2.08	1.99	1.81	1.99	1.90	
surplus $MgCO_3$	1.48	1.98	0.82	0.78	0.89	1.19	0.84	1.07	
Na:Cl	2.99	2.81	2.98	3.15	2.86	2.45	2.75	2.67	
beam amperage (nA)	5	5	3	3	3	3	3	3	
spot size (μm)	10	15	15	15	15	15	15	15	
				Unit Cell Parameters					
sample	*a* [Å]			R_{wp}			GOF		
CuR1B	14.05(2)			11.79			1.04		

[1] Comparative composition of northupite from [40], Searles Lake (California, USA) material; [2] Al, Fe, Mn, Zn, Sr, and K were analyzed but not detected; [3] backwards calculation from amount of CO_3^{2-} calculated based on stoichiometry and charge balance; [4] by stoichiometry and charge balance.

The unit cell parameters of juangodoyite from different samples vary only by up to 1%. Just in a single case—also in terms of the whole unit cell parameters calculated within the current study—the difference reaches 7%. The unit cell edges calculated for the different samples of chalconatronite are both similar to each other and to the synthetic material data. A maximum difference for the *β* angle is 0.14% (inter-sample comparison) or 0.57% (sample–literature data comparison). The malachite crystallography data also do not stand out. The unit cell parameters of aragonite show very low to low differences in both the intra-sample and sample–literature comparisons—the variations are expected due to the below-described substitutions. The data obtained for hydromagnesite and northupite are also very similar to those available in the literature ([40]). Although pure (as shown below), clinoatacamite shows slightly higher intra-sample variation ranges, being 1.1% for the parameter *β*. The unit cell parameters calculated for herbertsmithite of the samples CuR1A, CuR1B, and CuR6, are: *a* = 6.792(5) and *c* = 14.15(4) Å; *a* = 6.829(3) and *c* = 14.08(1) Å; and *a* = 6.821(2) and *c* = 14.063(7) Å, respectively. The crystallographical description of cornwallite is: *a* = 4.593(9), *b* = 5.703(2), *c* = 17.52(4), β = 92.72(16)°. The admixing in the sample CuR3a langite is characterized by the parameters *a* = 7.158(2), *b* = 6.08(2), and *c* = 11.33(12) Å, and β = 89.45(32)°. The eriochalcite unit cell is characterized by the unit cell parameters *a* = 7.44(4), *b* = 8.07(5), *c* = 3.74(4) Å (sample RSR9-1) and *a* = 7.490(9), *b* = 8.010(8), *c* = 3.725(3) Å (sample RSR9-3). The data for kröhnkite are: *a* = 5.795(5), *b* = 12.59(2), *c* = 5.541(8) Å, and β = 108.28(8)° (sample RSR9-1); *a* = 5.791(1), *b* = 12.614(2), *c* = 5.509(2) Å, and β = 108.44(2)° (sample RSR9-2). The parameters obtained for ktenasite and the lavendulan-group species are: *a* = 5.62(1), *b* = 6.10(1), *c* = 23.79(4) Å, and β = 95.87(2)°; *a* = 9.98(1), *b* = 19.633(5), *c* = 9.97(95) Å, and β = 90.86(95)°, respectively. The corresponding melanterite data are: *a* = 14.121(9), *b* = 6.475(4), *c* = 11.089(3) Å, and β = 105.76(33)°. Halite associating with aragonite has the unit cell parameter *a* = 5.6416(8) Å.

The value derived for halite present—together with possible traces of eriochalcite—in the matrix of chalconatronite and juangodoyite is $a = 5.9429(7)$ Å; and that for the material of the sample CuR6 is 5.6416(2) Å. The second-batch halite unit cell parameter a is equal to 5.6400(2) (sample RSR9-1) and 5.637(2) Å (sample RSR9-2).

Table 10. Results of the EPMA analyses of the Rudna IX clinoatacamite (analyses 1–6: CuR1B sample; analyses 7–12: CuR3 sample).

Analysis no.:	1	2	3	4	5	6	7	8	9	10	11	12
						wt.% [1]						
CuO	70.25	69.17	70.26	69.27	66.62	67.26	67.06	69.46	66.80	68.11	69.13	66.90
MgO	0.00	0.21	0.29	1.23	1.67	0.00	1.30	0.21	1.19	0.20	0.82	0.49
K_2O	0.00	0.00	0.00	0.00	0.00	0.00	0.00	0.00	0.12	0.07	0.00	0.00
Cl	16.14	16.06	15.29	13.83	13.36	16.10	15.99	15.60	14.79	15.92	15.13	15.56
Total-1	86.39	85.43	85.84	84.33	81.64	83.37	84.36	85.27	82.90	84.30	85.07	82.95
H_2O [2]	13.61	14.57	14.16	15.67	18.37	16.63	15.56	14.73	17.10	15.70	14.93	17.05
Total-2	100.00	100.00	100.00	100.00	100.00	100.00	100.00	100.00	100.00	100.00	100.00	100.00
						apfu [2 cations basis]						
Cu	2.00	1.99	1.98	1.93	1.91	2.00	1.93	1.99	1.93	1.99	1.95	1.97
Mg		0.01	0.02	0.07	0.09		0.07	0.01	0.07	0.01	0.05	0.03
K									0.01			
Cl	1.03	1.04	0.97	0.87	0.86	1.07	1.03	1.00	0.96	1.04	0.96	1.03
OH [3]	3.39	3.67	3.47	3.74	4.52	4.30	3.97	3.72	4.27	3.99	3.71	4.38
OH_N [4]	2.97	2.96	3.03	3.13	3.14	2.93	2.97	3.00	3.05	2.96	3.04	2.97
beam amperage (nA)	10	10	10	10	10	10	10	10	10	10	10	10
spot size (µm)	5	5	5	5	5	5	5	5	5	5	5	5

	Unit Cell Parameters					
sample	a [Å]	b [Å]	c [Å]	$β$ [°]	R_{wp}	GOF
CuR1A	6.148(3)	6.830(4)	9.153(5)	99.55(7)	11.79	1.04
CuR1B	6.18(5)	6.750(8)	9.06(2)	100.65(69)	12.14	1.09
RSR9-3	6.17(4)	6.80(3)	9.21(2)	100.27(49)	19.53	1.48

[1] Fe, Co, Ni, Zn, Pb, and Ca were analyzed but not detected; [2] by difference (100–Total-1); [3] by direct calculation from wt.% H_2O; [4] normalized content.

3.2.2. The Lubin Główny Minerals

The Lubin Główny rapidcreekite is chemically very pure (Table 11). Its empirical formula, based on 16 datapoints, is $Ca_{2.00}(SO_4)_{0.97}(CO_3)_{1.03}\cdot4.23H_2O$. The main component of the Lubin Główny assemblage—monohydrocalcite—is, as opposed to rapidcreekite, enriched in Cu, Zn, and possibly As. (Table 12). Most of the analyses were derived from a profile of datapoints, and the profile line was set in a microarea free of visible inclusions of the mentioned CuZnNiCoCa(MnMg) arsenate. However, juxtaposing As_2O_5-CuO, As_2O_5-ZnO, and CuO-ZnO (but not As_2O_5-SO_3) in a Pearson-correlation manner suggests strong positive trends, although not that evident for the As_2O_5-ZnO pair. As such, we suspect the monohydrocalcite itself of being devoid of As, and bearing small amounts of Zn, Cu, and S—as shown in Table 12. The analyses listed here concern spots with either lacking or minor As amounts.

The unit cell parameters calculated for rapidcreekite resemble those found in the literature (both References [31] and [40]). The same is true for monohydrocalcite. Slight difference in the latter case may be related to minor substitutions, as shown below. The relatively BSE-bright aragonite has the following unit cell parameters: $a = 4.9671(4)$, $b = 7.9763(6)$, and $c = 5.7534(5)$ Å (sample MS-Cu1); $a = 4.9616(8)$, $b = 7.969(2)$, and $c = 5.7466(8)$ Å (sample Cu4). The corresponding values for vaterite are: $a = 4.14(1)$, and $c = 8.41(2)$; $a = 4.089(3)$, and $c = 8.501(2)$ Å. The unit cell parameters of the minor, associated Cu hydrous sulfates of the sample MS-Cu1 are as follows: $a = 7.166(7)$, $b = 6.000(7)$, $c = 11.151(7)$ Å, $β = 87.73(9)°$ (langite); $a = 6.088(6)$, $b = 5.645(5)$, $c = 14.36(1)$ Å, $β = 117.59(7)°$ (wroewolfeite).

Table 11. Results of the EPMA analyses of the Lubin Główny rapidcreekite (sample Cu4).

Analysis no.:	1	2	3	4	5	6	7	8	9	10	11 [1]
					wt.% [2]						
SO_3	26.60	25.47	25.40	24.45	24.90	24.23	24.83	24.75	24.83	24.25	26.1
CuO	0.00	0.00	0.26	0.00	0.00	0.00	0.00	0.00	0.00	0.00	
CaO	38.51	36.35	36.48	35.86	36.07	36.11	36.04	36.48	36.31	36.61	36.3
Total-1	65.10	61.82	62.12	60.40	60.97	60.34	60.87	61.24	61.14	60,86	
CO_2 [3]	15.60	14.53	14.81	14.66	14.63	15.02	14.64	15.03	14.85	15.40	14.0
H_2O [4]	19.30	23.66	23.05	24.94	24.40	24.64	24.49	23.74	24.02	23.74	23.6
Total-2	100.00	100.00	100.00	100.00	100.00	100.00	100.00	100.00	100.00	100.00	100.00
					apfu [2 cations basis]						
SO_4^{2-}	0.97	0.98	0.97	0.96	0.97	0.94	0.97	0.95	0.96	0.93	
Cu			0.01								
Ca	2.00	2.00	1.99	2.00	2.00	2.00	2.00	2.00	2.00	2.00	
(CO_3^{2-}) [5]	1.03	1.02	1.03	1.04	1.03	1.06	1.03	1.05	1.04	1.07	
H_2O [6]	3.11	4.04	3.91	4.32	4.20	4.24	4.22	4.04	4.11	4.03	
beam amperage (nA)	10	10	10	10	10	10	10	10	10	10	
spot size (µm)	10	15	15	15	15	15	15	15	15	15	
					Unit Cell Parameters						
sample	*a* [Å]		*b* [Å]		*c* [Å]		R_{wp} [%]		GOF [%]		
Cu4	15.505(3)		19.22(2)		6.165(2)		16.46		1.37		

[1] Comparative composition from [25], type-locality material; [2] only the non-zero records reported; [3] backward calculation after setting amount of CO_3^{2-} by charge balance and stoichiometry; [4] by difference (100–Total-1-wt.% CO_2); [5] by charge balance and stoichiometry; [6] by direct calculation from wt.% H_2O.

Table 12. Results of the EPMA analyses of the Lubin Główny cuprian-zincian monohydrocalcite (sample Cu4).

Analysis no.:	1	2	3	4	5	6	7	8	9	10	11
As_2O_5	0.80	0.56	0.25	0.00	0.00	0.00	0.00	0.00	n.a.	n.a.	n.a. [1]
P_2O_5	0.00	0.00	0.00	0.00	0.00	0.00	0.00	0.00	0.00	0.00	0.00
SO_3	0.33	0.37	0.57	0.38	0.41	0.41	0.39	0.42	0.50	0.47	0.62
SiO_2	0.00	0.00	0.00	0.00	0.00	0.00	0.00	0.00	0.00	0.00	0.00
Al_2O_3	0.00	0.00	0.00	0.00	0.00	0.00	0.00	0.00	0.00	0.00	0.00
FeO	0.00	0.00	0.00	0.00	0.00	0.00	0.00	0.00	0.00	0.00	0.00
MnO	0.00	0.00	0.00	0.00	0.00	0.00	0.00	0.00	0.00	0.00	0.00
CuO	3.53	3.01	2.37	0.42	1.95	0.32	1.47	1.21	0.97	1.55	1.55
ZnO	0.34	0.53	0.59	0.00	0.00	0.00	0.00	0.00	0.00	0.00	0.00
MgO	0.00	0.00	0.00	0.00	0.00	0.00	0.00	0.00	0.00	0.00	0.00
CaO	41.77	42.50	41.83	45.93	43.59	45.03	44.43	44.18	43.96	42.34	42.59
SrO	0.00	0.00	0.00	0.00	0.00	0.00	0.00	0.00	0.00	0.00	0.00
Na_2O	0.00	0.00	0.00	0.00	0.00	0.00	0.00	0.00	0.00	0.00	0.00
K_2O	0.00	0.00	0.00	0.00	0.00	0.00	0.00	0.00	0.00	0.00	0.00
Total-1	46.75	46.96	45.60	46.73	45.96	45.76	46.29	45.81	45.44	44.36	44.76
CO_2 [1]	34.50	34.94	34.07	36.08	35.07	35.29	35.47	35.11	34.77	33.83	33.95
Total-2	81.26	81.90	79.68	82.81	81.02	81.06	81.76	80.93	80.20	78.19	78.70
					apfu [1 cation basis]						
SO_4^{2-}	0.01	0.01	0.01	0.01	0.01	0.01	0.01	0.01	0.01	0.01	0.01
Cu	0.06	0.05	0.04	0.01	0.03	0.01	0.02	0.02	0.02	0.03	0.02
Zn	0.01	0.01	0.01								
Ca	0.94	0.94	0.95	0.99	0.97	0.99	0.98	0.98	0.98	0.97	0.98
(CO_3^{2-}) [2]	0.99	0.99	0.99	0.99	0.99	0.99	0.99	0.99	0.99	0.99	0.99
beam amperage (nA)	10	10	10	10	10	10	10	10	10	10	10
spot size (µm)	10	10	10	10	10	10	10	10	10	10	10
					Unit Cell Parameters						
sample	*a* [Å]		*c* [Å]		R_{wp} [%]				GOF [%]		
MS-Cu1	10.564(2)		7.548(3)		16.00				1.33		
Cu4	10.5512(9)		7.5483(1)		16.46				1.37		

[1] Not analyzed; [2] backward calculation from amount of CO_3^{2-} set as ideal content.

The arsenate phase either forms very thin, ribbon-like, curved veinlets within monohydrocalcite-aragonite aggregates, or tiny (up to ~60 μm in length) crystals included in rapidcreekite (Figure 6e). However, compact aggregates, up to 20 μm thick, covering aragonite (Figure 6f) are more frequent. The analyses of the arsenate phase are to be found in Table 13. The manipulation of the measurement conditions, both the beam current and size, does not impact any larger changes in the wt.% results. Two slightly different crystallochemical types of the species were identified, coming from two separate fragments of the dripstone material. The first one (analyses 1–5) is slightly more cuprian (31.59 wt.% versus 26.13 wt.% CuO) and arsenian (20.23 wt.% versus 18.59 wt.% As_2O_5), but less calcian (4.02 versus 6.58 wt.% CaO) than the second variety. The latter, coming from a dolomite-rich sample, is also characterized by a slightly elevated average SiO_2 content—0.38 wt.% as compared to 0.25—and may bear more Na. It is also slightly more magnesian (mean 0.59 wt.% MgO against 0.44) and clearly more calcian (mean 6.58 wt.% CaO against 4.02). Both varieties show similar SO_3 concentration: ~0.26 wt.% SO_3. The ZnO, NiO, CoO, MgO, and SiO_2 concentrations are also close, being 16.02 and 17.64; 1.22 and 1.26; 1.25 and 1.34; 0.44 and 0.59; and 0.25 and 0.38, respectively. The first variety seems to be more mangani- and stibiferous. Phosphorus is an occasional guest in the structure.

Table 13. Results of the EPMA analyses of the Lubin Główny CuZnNiCoCa(MnMg) arsenate phase (analyses 1–5: first microarea; analyses 6–9; second microarea).

Analysis no.:	1	2	3	4	5	6	7	8	9
					wt.% [1]				
As_2O_5	19.78	20.41	19.75	20.53	20.67	16.90	19.66	17.60	20.22
Sb_2O_5	0.00	0.22	0.19	0.21	0.19	0.15	0.16	0.00	0.17
P_2O_5	0.00	0.12	0.00	0.00	0.17	0.11	0.00	0.00	0.00
SO_3	0.35	0.29	0.29	0.18	0.25	0.27	0.43	0.22	0.11
SiO_2	0.25	0.21	0.28	0.23	0.27	0.36	0.38	0.38	0.39
MnO	0.00	0.37	0.35	0.33	0.33	0.42	0.00	0.00	0.00
CuO	29.70	33.60	30.71	32.24	31.68	24.48	26.18	25.35	28.51
ZnO	16.01	15.59	16.57	15.86	16.05	19.60	17.08	16.90	16.99
CoO	1.31	1.12	1.35	1.11	1.34	1.48	1.32	1.35	1.22
NiO	1.17	1.08	1.47	1.01	1.37	1.41	1.10	1.14	1.39
MgO	0.49	0.40	0.39	0.48	0.42	0.53	0.62	0.58	0.64
CaO	4.36	3.86	4.33	3.77	3.76	5.59	5.70	8.55	6.47
Na_2O	0.00	0.00	0.00	0.51	0.48	0.58	0.52	0.75	0.00
Total-1	73.41	77.27	75.68	76.46	76.99	71.87	73.16	72.81	76.09
H_2O [2]	26.59	22.73	24.32	23.54	23.01	28.13	26.85	27.19	23.91
Total-2	100.00	100.00	100.00	100.00	100.00	100.00	100.00	100.00	100.00
					apfu [9 cations basis]				
AsO_4^{3-}	2.23	2.20	2.15	2.21	2.22	1.83	2.18	1.84	2.16
SiO_4^{4-}	0.05	0.04	0.06	0.05	0.06	0.07	0.08	0.08	0.08
SbO_4^{3-}		0.02	0.01	0.02	0.01	0.01	0.01		0.01
PO_4^{3-}		0.02			0.03	0.02			
SO_4^{2-}	0.06	0.04	0.05	0.03	0.04	0.04	0.07	0.03	0.02
Mn		0.07	0.06	0.06	0.06	0.07			
Cu	4.85	5.23	4.83	5.01	4.91	3.82	4.20	3.82	4.40
Zn	2.55	2.37	2.55	2.41	2.43	2.99	2.68	2.49	2.56
Co	0.23	0.18	0.23	0.18	0.22	0.25	0.23	0.22	0.20
Ni	0.20	0.18	0.25	0.17	0.23	0.23	0.19	0.18	0.23
Mg	0.16	0.12	0.12	0.15	0.13	0.16	0.20	0.17	0.19
Ca	1.01	0.85	0.97	0.83	0.83	1.24	1.30	1.83	1.42
Na				0.20	0.19	0.23	0.21	0.29	
H	38.26	31.16	33.72	32.22	31.47	38.71	37.96	36.13	32.52
beam amperage (nA)	10	10	10	10	10	10	5	5	5
spot size (μm)	5	5	5	5	5	6	7	5	"0"

[1] Al, Fe, Sr, Pb, K, and Cl were analyzed but not detected; [2] by difference (100–Total-1).

The mineral studied could not be recast to any of the 36 currently known, accepted or questionable Cu arsenate minerals. The chemical composition and, possibly, stoichiometry resembles that of sabelliite, $(Cu,Zn)_2Zn(AsO_4,SbO_4)(OH)_3$, or parnauite, $Cu_9(AsO_4)_2(SO_4)(OH)_{10} \cdot 7H_2O$. Recasting the mineral to sabelliite (3 cations factor basis) requires an assumption of CO_3^{2-} substitution for balancing both the charge and tetrahedral (*T*) site occupancy (as, e.g., in the apatite supergroup; e.g., [45]). The *T*-site occupancy balance cannot be assured by OH^- substitution, i.e., protonation of the AsO_4^{3-} ion, as it would not allow for maintaining neutral charge. Nominally unknown in sabellite carbonate, substitution is possible in the structure of parnauite [46]. Recasting to parnauite (nine cations basis) gives the following, corresponding formulas: $(Cu_{4.97}Zn_{2.46}Ca_{0.90}Co_{0.21}Ni_{0.20}Mg_{0.14}Na_{0.08}Mn_{0.05})_{\Sigma 9.01}(AsO_4)_{2.00}[(CO_3)_{0.69}(AsO_4)_{0.20}(SiO_4)_{0.05}(SO_4)_{0.04}(PO_4)_{0.01}(SbO_4)_{0.01}]_{\Sigma 1.00}$ $(OH)_{9.62} \cdot 11.87H_2O$ (first variety) and $(Cu_{4.06}Zn_{2.68}Ca_{1.44}Co_{0.22}Ni_{0.21}Mg_{0.18}Na_{0.18}Mn_{0.02})_{\Sigma 8.99}(AsO_4)_{2.00}$ $[(CO_3)_{0.83}(SiO_4)_{0.08}(SO_4)_{0.04}(SbO_4)_{0.01}]_{\Sigma 1.00}(OH)_{9.71} \cdot 13.31H_2O$ (second variety). Assuming surplus H_2O erroneously derived from sample destruction, the mineral under scope could represent the carbonate analogue of parnauite. A trial of recasting the Lubin arsenate to "debaoite", $Cu_9(AsO_4)_2(SO_4)(OH,CO_3)_{10} \cdot 6H_2O$—a supposed "variety" of parnauite [47]—allows us to write the atomic representation as $(Cu_{4.97}Zn_{2.46}Ca_{0.90}Co_{0.21}Ni_{0.20}Mg_{0.14}Na_{0.08}Mn_{0.05})_{\Sigma 9.01}[(AsO_4)_{2.20}$ $(SiO_4)_{0.05}(SO_4)_{0.04}(PO_4)_{0.01}(SbO_4)_{0.01}]_{\Sigma 2.31}[(OH)_{9.10}(CO_3)_{0.10}]_{\Sigma 10.00} \cdot 12.13H_2O$ (first variety) and $(Cu_{4.06}Zn_{2.68}Ca_{1.44}Co_{0.22}Ni_{0.21}Mg_{0.18}Na_{0.18} \ Mn_{0.02})_{\Sigma 8.99}[(AsO_4)_{2.00}(SiO_4)_{0.08}(SO_4)_{0.04}(SbO_4)_{0.01}]_{\Sigma 2.13}$ $[(OH)_{8.63}(CO_3)_{1.37}]_{\Sigma 10.00} \cdot 13.85H_2O$ (second variety).

The mineral under scope gives relatively good recast results with a total four-cation factor basis: $(Cu_{2.21}Zn_{1.09}Ca_{0.40}Ni_{0.09}Co_{0.09}Mg_{0.07}Na_{0.04}Mn_{0.02})_{\Sigma 4.01}[(AsO_4)_{0.98}(SiO_4)_{0.02}(SO_4)_{0.02}(SbO_4)_{0.01}]_{\Sigma 1.03}$ $OH)_{4.85} \cdot 4.99H_2O$ (first variety) and $(Cu_{2.21}Zn_{1.09}Ca_{0.40}Ni_{0.09}Co_{0.09}Mg_{0.07}Na_{0.04}Mn_{0.02})_{\Sigma 4.01}[(AsO_4)_{0.98}$ $(SiO_4)_{0.02}(SO_4)_{0.02}(SbO_4)_{0.01}]_{\Sigma 1.03}OH)_{4.85} \cdot 4.99H_2O$ (second variety), with close-to-integer site occupancies not requiring CO_3^{2-} substitution. As such, the proposed formulas possibly correspond to the $(Cu,Zn,Ca,Ni,Co)_4(AsO_4)(OH)_5 \cdot 5H_2O$ or $Cu_2(Zn,Ca,Cu)_2(AsO_4)(OH)_5 \cdot 5H_2O$ ideal ones. We are aware that the correct identification of the nature of this species requires confirmation of the occurrence of the CO_3^{2-}, e.g., via μRaman spectroscopy, and a detailed structural analysis.

4. Discussion

The holotype (i.e., type-locality) juangodoyite, as described by [1], was found to be "bright ultramarine", fine pseudomorphs after chalconatronite laths, with individuals as small as up to 5 μm in diameter. The Chilean mineral is also associated with sanrománite, $Na_2CaPb(CO_3)_5$, malachite, calcite, anhydrite, trona, $Na_3(CO_3)(HCO_3) \cdot 2H_2O$, and nahcolite, $NaHCO_3$. Although we do observe pseudomorphisation in the juangodoyite-chalconatronite system, non-pseudomorphosed chalconatronite crystals are also observed. This relates to both the azure-coloured, spear-like crystals and the teal-coloured, dioptase-like crystals. The Chilean juangodoyite is said to readily hydrate to chalconatronite—a process lasting several hours. We do not observe such changes—in a macroscopic view—in our material. Such changes may, however, be hidden due to their possible microscale character. Also, the very dark, azure-like colour of our chalconatronite crystals is somewhat remarkable and is related to some difficulties in distinguishing the particular Na-Cu carbonate phase. A planned single-crystal study is expected to resolve such issues.

As in the case of the Rudna material, the holotype juangodoyite is very pure, with 28.27 wt.% Na_2O, 33.77 wt.% CuO, and 38.45 wt.% CO_2, corresponding to $Na_{2.08}Cu_{0.98}(C_{1.99}O_6)$ empirical formula. The chalconatronite holotype has [in wt%]: 20.0 Na_2O, 26.8 CuO, 29.5 CO_2, 20.4 H_2O, 2.8 PbO (impurity from Cu-Sn bronze), 0.5 SiO_2, and 0.6 R_2O_3 (R = Al, Fe, . . .) [4]. The Jáchymov material of [9] associated with pirssonite, $Na_2Ca(CO_3)_2 \cdot 2H_2O$, or gaylussite, $Na_2Ca(CO_3)_2 \cdot 5H_2O$, is slightly impure, as shown by the empirical formula: $Na_{2.01}(Cu_{0.98}Fe_{0.01})_{\Sigma 0.99}[(CO_3)_{1.95}(PO_4)_{0.02}(AsO_4)_{0.01}(SiO_4)_{0.01}]_{\Sigma 0.99} \cdot 3H_2O$.

According to [48], chalconatronite (or rather its synthetic equivalent) is formed at the expense of copper alloy artefacts exposed to Na_2CO_3 solutions in air, or via the interaction of the artefacts with soda glass. The Rudna IX Na-Cu carbonates were likely formed via an interaction of saline, CO_2-rich

(and thus possibly also Na_2CO_3-saturated) mine waters with chalcocite, tennantite, and other Cu ore minerals undergoing weathering.

The holotype rapidcreekite is not the only product of surface weathering. The other minerals of this genesis include aragonite, gypsum, hydromagnesite, nesquehonite, and jarosite-group species [25]. The Diana Cave rapidcreekite occurs in a fault line with a hot spring (51 °C on average). The spring waters are almost pH-neutral and rich in SO_4^{2-}, Cl^-, Na^+, and Ca^{2+} ions [31]. Such a description in reminiscent of the seepage phenomenon observed in the Lubin Główny mine. The Diana Cave rapidcreekite is slightly impure, with an empirical formula given as $(Ca_{1.98}Na_{0.03}Mg_{0.01})_{\Sigma 1.02}(S_{0.97}O_4)(C_{0.97}O_3) \cdot 4H_2O$ and additional Al admixture of 0.07 wt.%, oxide basis. The authors mentioned that their rapidcreekite analysis is second to date, only. The following reactions, starting from H_2SO_4, were suggested by them to lead to rapidcreekite crystallization:

$$2H^+ + SO_4^{2-} + 2CaCO_3 + 2H_2O \rightarrow Ca^{2+} + 2HCO_3^- + CaSO_4 \cdot 2H_2O \qquad (1)$$

$$Ca_xNa_{x-1}(CO_3)_y(SO_4)_{1-y} \leftrightarrow xCa^{2+} + (1-x)Na^+ + yCO_3^{2-} + (1-y)SO_4^{2-} \qquad (2)$$

$$3Ca^{2+} + 2HCO_3^{2-} + SO_4^{2-} + 3H_2O \rightarrow Ca_2(SO_4)(CO_3) \cdot 4H_2O + \text{"}CaCO_3\text{"} \qquad (3)$$
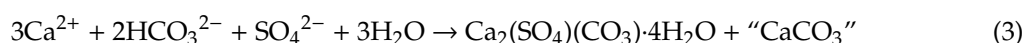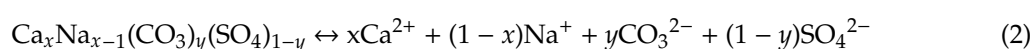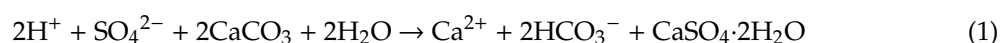
The second reaction concerns equilibrium between CO_3^{2-} (solution), SO_4^{2-} (solution) and CO_3-SO_4-bearing solid(s), derived from [44]. The [44] team also cited [49,50] who dealt with rapidcreekite crystallization conditions, e.g., during nanofiltration of saturated $CaSO_4$ solution in the presence of CO_3^{2-} ions. According to these authors, rapidcreekite, as a phase more soluble than calcite, needs lower aCO_3^{2-} to precipitate. Example activity conditions favouring rapidcreekite crystallization were described with a CO_3^{2-}/SO_4^{2-} ratio of 4.5×10^{-3}. Rapidcreekite crystallization at the Diana Cave is suggested to take place at pH > 6.4 (i.e., above gypsum precipitation conditions) and CO_3^{2-}/SO_4^{2-} ratio of 0.06–0.46. As such, the stability range of rapidcreekite is narrow, as also confirmed by the abundance of gypsum and calcite in the Lubin samples, suggestive of variations in the local conditions. The rapidcreekite crystallization window is located between the preceding gypsum and postdating $CaCO_3$ crystallization stages. Interestingly, the "$CaCO_3$" phase of the third reaction was interpreted by Onac's team [44] as aragonite or vaterite—both also present in Lubin. Indeed, these two $CaCO_3$ polymorphs are stabilized by Mg^{2+} ions contained in solutions. Such ions may have easily been mobilized from the Lubin dolostones.

The Na-Cu carbonate paragenesis from the Rudna IX mine most likely formed due to an interaction of saline and/or sodic and carbonaceous mine waters with the copper ores. The rapidcreekite- and $CaCO_3$-bearing dripstones of the Lubin Główny mine undoubtedly resulted from an interaction of the local, warm mine water seepage, with wall-forming rocks. Such outflows' waters were also studied by [51] who reported them as weakly mineralized, SO_4^{2-}-CO_3^{2-} ones, with dissolved NaCl content increasing with depth. Calcium and carbonate ions may have been either derived from the seepage or from dolostone, while sulfate ions may have been derived from seepage or Cu sulfide ore weathering. Copper, nickel, cobalt, and arsenic were mobilized from arsenide and sulfarsenide ores disseminated within the dolostone. The most probable source of Mn is both the dolostone and local calcite fillings. We have confirmed the Mn enrichment of this calcite.

Although the stochiometry and structural nature of the rapidcreekite-associated arsenate species remain unknown, the proposed CO_3^{2-} substitution has an important argument: the simultaneous Na enrichment of the mineral. The inclusion of Na^+ induces a drop in positive charge. The sole occupancy of the *T* site by AsO_4^{3-} and SiO_4^{4-} group would cause surplus negative charge. The presented microchemical data for malachite are similar, as the Na presence reported is repetitive. The charge may be balanced by the CO_3^{2-}. Coupled Na^+ and CO_3^{2-} substitution in the mentioned apatite group is reported by [45]. This, however, concerns the easily substituted Na^+-Ca^{2+} pair. As opposed to that, Na-Cu diadochy is almost unknown among minerals, with exceptions in channel sites in piypite (e.g., [52]) and to some extent in barahonaite-group minerals (e.g., [53]). The same is true for K-Cu pair, which is only confirmed in channels of aleutite [54]. A (Zn,Na,Cu,Mg) diadochy is also known in

majzlanite [55]. Nevertheless, possible Na-Cu and K-Cu substitution systems in our minerals need further studies to be confirmed or disproved.

References

1. Schlüter, J.; Pohl, D. Juangodoyite, $Na_2Cu(CO_3)_2$, a new mineral from the Santa Rosa mine, Atacama desert, Chile. *Neues Jahrb. Mineral. Abh.* **2005**, *182*, 11–14.

2. Maslen, E.N.; Spadaccini, N.; Watson, K.J. Electron Density in Non-Ideal Metal Complexes. II Sodium Bis(carbonato)cuprate(II). *Acta Cryst.* **1986**, *B42*, 430–436. [CrossRef]

3. Mosset, A.; Bonnet, J.-J.; Galy, J. Structure cristalline de la chalconatronite synthétique: $Na_2Cu(CO_3)_2 \cdot 2H_2O$. *Zeits. Krist.* **1978**, *148*, 165–177. (In French with English Abstract) [CrossRef]

4. Carbone, C.; Dinelli, E.; De Waele, J. Characterization of minothems at Libiola (NW Italy): Morphological, mineralogical, and geochemical study. *Int. J. Spel.* **2016**, *45*, 171–183. [CrossRef]

5. Frondel, C.; Gettens, R.J. Chalconatronite, a new mineral from Egypt. *Science* **1955**, *122*, 75–76. [CrossRef]

6. Dini, M.; Schlüter, J.; Malcherek, T.; Pohl, D. Sanrománite, from the Santa Rosa mine, Atacama desert, Chile, a new mineral of the burbankite group. *Neues Jahrb. Mineral. Abh.* **2007**, *183*, 117–121.

7. Sciberras, M.J.; Leverett, P.; Williams, P.A.; Hibbs, D.E.; Downes, P.J.; Welch, M.D.; Kampf, A.R. Paratacamite-(Ni), $Cu_3(Ni,Cu)Cl_2(OH)_6$, a new mineral from the Carr Boyd Rocks mine, Western Australia. *Austr. J. Miner.* **2013**, *17*, 39–44.

8. Pichler, A. *Bergbau in Westkärnten, eine Bestandsaufnahme der Noch Sichtbaren Merkmale der Historischen Bergbaue in Westkärnten*; Verlag des Naturwissenschaftlichen Vereins für Kärnten: Klagendurt, Austria, 2009; Volume 63, p. 416. (In German)

9. Plášil, J.; Hloušek, J.; Škoda, R. Chalkonatronit, $Na_2Cu(CO_3)_2(H_2O)_3$, ze žíly sv. Ducha, Jáchymov (Česká republika) [Chalconatronite, $Na_2Cu(CO_3)_2(H_2O)_3$, from the "sv. Duch" vein, Jáchymov (Czech Republic)]. *Bull. Miner.-Petrolog. Odd. Nár. Muz. (Praha)* **2013**, *21*, 228–233. (In Czech)

10. Stalder, H.A.; Wagner, A.; Graeser, S.; Stuker, P. *Mineralienlexikon der Schweiz*; Wepf Verlag: Basel, Switzerland, 1998; p. 106.

11. Weiss, S. *Mineralfundstellen, Deutschland West*; Christian Weise Verlag: München, Germany, 1990; p. 320. (In German)

12. Wittern, A.; Schnorrer-Köhler, G. Die Minerale der Glücksrad-Halde bei Oberschulenberg/Harz. *Lapis* **1986**, *11*, 9.

13. Schnorrer-Köhler, G.; David, W. Die Blei-und Silberhütte Braubach und ihre Haldenminerale. *Lapis* **1991**, *16*, 38–53, 58.

14. Dietrich, R.; Bode, R. Famous Mineral Localities: The Mines and Minerals of Bad Ems [Germany]. *Mineral. Rec.* **1984**, *15*, 323–344.

15. Lahl, B. Berühmte Annaberger Gruben und ihre Geschichte. *Lapis* **1992**, *17*, 34–38. (In German)

16. Eckel, E.B. *Minerals of Colorado*; Fulcrum Publishing: Golden, CO, USA, 1997; p. 676.

17. Heinrich, E.W.; Robinson, G.W. *Mineralogy of Michigan*, 1st ed.; Michigan Technical University: Houghton, MI, USA, 2004; p. 252.

18. Rosemeyer, T. The Kearsarge: Copper-bearing Amygdaloidal Lode, Houghton and Keweenaw Counties, Michigan. *Rocks Miner.* **2007**, *82*, 276–297. [CrossRef]

19.   Rosemeyer, T. The History, Geology, and Mineralogy of the White Pine Mine, Ontonagon County, Michigan. *Rocks Miner.* **1999**, *74*, 160–176. [CrossRef]

20.   Kampf, A.R.; Plášil, J.; Kasatkin, A.V.; Marty, J.; Čejka, J. Markeyite, a new calcium uranyl carbonate mineral from the Markey mine, San Juan County, Utah, USA. *Mineral. Mag.* **2018**, *82*, 1089–1100. [CrossRef]

21.   Desor, J. New Minerals from the Eureka Mine. 2018. Available online: http://mineralanalytik.de/images/REMBILDER/march18-02.pdf (accessed on 20 December 2018).

22.   Lafuente, B.; Downs, R.T.; Yang, H.; Stone, N. The power of databases: The RRUFF project. In *Highlights in Mineralogical Crystallography*; Armbruster, T., Danisi, R.M., Eds.; De Gruyter: Berlin, Germany, 2015; pp. 1–30.

23.   Cooper, M.A.; Hawthorne, F.C. The crystal structure of rapidcreekite, $Ca_2(SO_4)(CO_3)(H_2O)_4$, and its relation to the structure of gypsum. *The Can. Mineral.* **1996**, *34*, 99–106.

24.   Bots, P. Experimental Investigation of Calcium Carbonate Mineralogy in Past and Future Oceans. Ph.D. Thesis, School of Earth and Environment, University of Leeds, Leeds, UK, 2011; 212p.

25.   Roberts, A.C.; Ansell, H.G.; Jonasson, I.R.; Grice, J.D.; Ramik, R.A. Rapidcreekite, a new hydrated calcium sulfate-carbonate from the Rapid Creek area, Yukon Territory. *Can. Mineral.* **1986**, *24*, 51–54.

26.   Van Velthuizen, J.; Sturman, D.; Robinson, G.W.; Ansell, H.G. Mineralogy of the Rapid Creek and Bigh Fish River Area, Yukon Territory. *Mineral. Rec.* **1992**, *23*, 1–47.

27.   Walenta, K.; Dunn, P.J. Camgasite, a new calcium-magnesium arsenate mineral with composition $CaMg(AsO_4)(OH) \cdot 5H_2O$ from Wittichen in the Central Black Forest. *Der Aufschluss* **1989**, *40*, 369–372, (in German with English abstract).

28.   Rüger, F.; Senf, L.; Witzke, T. Die Saalfelder Feengrotten: Seltene Sekundärmineralien aus Thüringen. *Lapis* **1995**, *20*, 15–26.

29.   Rieck, B.; Kolitsch, U.; Voudouris, P.; Giester, G.; Tzeferis, P. Wietere Neufunde aus Lavrion, Griechenland. *Miner.-Welt* **2018**, *29*, 32–77. (In German)

30.   Raade, G. Etter Neumann. *NAGS-nytt* **1989**, *16*, 49.

31.   Onac, B.P.; Effenberger, H.S. Rapidcreekite, $Ca_2(SO_4)(CO_3) \cdot 4H_2O$, in the H_2S-rich environment of Diana Cave (Romania). In Proceedings of the 20th General Meeting of the IMA (IMA2010), Budapest, Hungary, 21–27 August 2010; p. 470, CD of Abstracts.

32.   Salama, W.; Ciobota, V.; El Aref, M.; Gaupp, R. Identification of mineralogy and organic materials of the Cretaceous and Middle Eocene ironstones by means of FTIR and micro-Raman spectroscopy. In Proceedings of the 7th European Conference on Mineralogy and Spectroscopy, ECMS, Potsdam, Germany, 4–7 September 2011. Document no. 27308.

33.   Warchulski, R.; Gawęda, A.; Kądziołka-Gaweł, M.; Szopa, K. Composition and element mobilization in pyrometallurgical slags from the Orzeł Biały smelting plant in the Bytom-Piekary Śląskie area, Poland. *Mineral. Mag.* **2015**, *79*, 459–484. [CrossRef]

34.   Oszczepalski, P.; Speczik, S.; Małecka, K.; Chmielewski, A. Prospective copper resources in Poland. *Gosp. Sur. Miner. (Miner. Res. Manag.)* **2016**, *32*, 5–30. [CrossRef]

35.   Nieć, M.; Piestrzyński, A. Forma i budowa złoża (Shape and laying of the deposit). In *Monografia KGHM Polska Miedź S.A. (a, Monograph)*; Piestrzyński, A., Ed.; KGHM Cuprum, CBR: Lubin, Poland, 2007; pp. 157–163. (In Polish)

36.   Harańczyk, C.; Jarosz, J. Ore minerals from copper deposit in Fore-Sudetic Monocline. *Rudy i Metale* **1973**, *6*, 493–498. (In Polish)

37.   Kucha, H. Ore mineralogy and geochemistry of ore body at Lubin-Sieroszowice deposit. *Biul. PIG* **2007**, *423*, 77–94. (In Polish with English Abstract)

38.   Siuda, R.; Łodziński, M.; Syczewski, M.; Kruszewski, Ł.; Pršek, J.; Hoffman, P. The first botallackite occurrence in Poland (Polkowice-Sieroszowice mine). *Biul. PIG* **2017**, *469*, 217–228. (In Polish with English Abstract) [CrossRef]

39.   Kruszewski, Ł.; Siuda, R.; Świek, M.; Szełęg, E. New occurrences of secondary minerals from Fore-Sudetic Monocline copper deposits: Juangodoyite (Rudna IX mine) and rapidcreekite/brushite (Lubin Główny mine). *Min. Spec. Pap.* **2019**, *46*, 55.

40.   O'Connor, V.A. Comparative Crystal Chemistry of Hydrous Iron Sulfates from Different Terrestrial Environments. Bachelor's Thesis, Department of Geology, Smith College, Northampton, MA, USA, 2005; p. 150.

41.	Anthony, J.W.; Bideaux, R.A.; Bladh, K.W.; Nichols, M.C. (Eds.) Borates, Carbonates, Sulfates. In *Handbook of Mineralogy*; Mineralogical Society of America: Chantilly, VA, USA, 2003; Volume 5, p. 791.

42.	Kucha, H.; Piestrzyński, A.; Wieczorek, A. Copper-bearing glauconite from the Weissliegendes of Zechstein copper deposits, Poland. *Min. Pol.* **1982**, *13*, 21–26.

43.	Kucha, H. Felspars, clay, organic and carbonate receptors of heavy metals in Zechstein deposits (Kupferschiefer type), Poland. *Trans. Inst. Min. Metall. (Sec. B Appl. Earth Sci.)* **1985**, *94*, 133–146.

44.	Busenberg, E.; Plummer, N.L. Kinetic and thermodynamic factors controlling the distribution of SO_4^{2-} and Na^+ in calcites and selected aragonites. *Geochim. Cosmochim. Acta* **1985**, *49*, 713–725. [CrossRef]

45.	Fleet, M.E.; Liu, X. Coupled substitution of type A and B carbonate in sodium-bearing apatite. *Biomater.* **2007**, *28*, 916–926. [CrossRef] [PubMed]

46.	Anthony, J.W.; Bideaux, R.A.; Bladh, K.W.; Nichols, M.C. (Eds.) Arsenates, Phosphates, Vanadates. In *Handbook of Mineralogy*; Mineralogical Society of America: Chantilly, VA, USA, 2000; Volume 4, p. 680.

47.	Li, Y.; Lai, L. Preliminary study of the characteristics and the genesis of arsenate minerals in the oxidized zone of the Debao skarn-type Cu-Sn ore deposit in Guangxi. *Acta Geol. Sin.* **1990**, *64*, 337–343. (In Chinese with English Abstract)

48.	Fischer, A.; Eggert, G.; Stelzner, J. When Glass and Metal Corrode Together, VI: Chalconatronite. *Stud. Conser.* 2019. [CrossRef]

49.	Dydo, P.; Turek, M.; Ciba, J. Scaling analysis of nanofiltration systems fed with saturated calcium sulfate solutions in the presence of carbonate ions. *Desalination* **2003**, *159*, 245–251. [CrossRef]

50.	Schausberg, P.; Mustafa, G.M.; Leslie, G.; Friedl, A. Scaling prediction based on thermodynamic equilibrium calculation—Scopes and limitations. *Desalination* **2009**, *244*, 31–47. [CrossRef]

51.	Kleczkowski, A.S.; Downorowicz, S.; Zimny, W.; Becker, R. Hydrogeologia serii złożowej (Ore series hydrogeology). In *Monografia KGHM, Polska Miedź SA*; Piestrzyński, A., Ed.; KGHM Cuprum, CBR: Lubin, Poland, 2007; pp. 133–138.

52.	Pekov, I. *Minerals First Discovered on the Territory of the Former Soviet Union*; Ocean Pictures: Moscow, Russia, 1998; p. 369.

53.	Viñals, J.; Jambor, J.L.; Raudsepp, M.; Roberts, A.C.; Grice, J.D.; Kokinos, M.; Wise, W.S. Barahonaite-(Al) and barahonaite-(Fe) new Ca-Cu arsenate mineral species, from Murcia Province, southeastern Spain, and Gold Hill, Utah. *Can. Mineral.* **2008**, *46*, 205–217. [CrossRef]

54.	Siidra, O.I.; Nazarchuk, E.; Agakhanov, A.A.; Polekhovsky, Y.S. Aleutite, IMA 2018-014. *Mineral. Mag.* **2018**, *82*, 779–785.

55.	Siidra, O.I.; Nazarchuk, E.; Zaitsev, A.N.; Shilovskikh, V.V. Majzlanite, $K_2Na(ZnNa)Ca(SO_4)_4$, a new anhydrous sulphate mineral with complex cation substitutions from Tolbachik volcano. *Mineral. Mag.* **2019**. [CrossRef]